

Isospin-violating vacuum polarization in the muon $(g - 2)$ with $SU(3)$ flavour symmetry from lattice QCD

Dominik Erb,^a Antoine Gérardin,^b Harvey B. Meyer,^{a,c} Julian Parrino,^d
Volodymyr Biloshytskyi,^e and Vladimir Pascalutsa^e

^a*PRISMA⁺ Cluster of Excellence & Institut für Kernphysik, Johannes Gutenberg-Universität Mainz, D-55099 Mainz, Germany*

^b*Aix-Marseille Université, Université de Toulon, CNRS, CPT, Marseille, France*

^c*Helmholtz Institut Mainz, Staudingerweg 18, D-55128 Mainz, Germany*

^d*Universität Regensburg, Fakultät für Physik, Universitätsstraße 31, 93040 Regensburg, Germany*

^e*Institut für Kernphysik, Johannes Gutenberg-Universität Mainz, D-55099 Mainz, Germany*

E-mail: domerb@uni-mainz.de

ABSTRACT: We compute the isospin-violating part $a_\mu^{\text{HVP},38}$ of the hadronic-vacuum-polarization (HVP) contribution to the muon $(g - 2)$ in lattice QCD at the $SU(3)_f$ -symmetric point where $M_\pi = M_K \simeq 416$ MeV. All diagrams involving internal photons are evaluated in coordinate space, employing a Pauli-Villars-regulated photon propagator with a cutoff scale Λ well below the lattice cutoff. The counterterm $(m_u - m_d)$, whose Λ dependence is consistent with the expected logarithmic behaviour, is calibrated using the experimental kaon mass splitting as input. The bare electromagnetic contribution at fixed Λ is compared to a phenomenological estimate based on the kaon-loop and pseudoscalar-pole contributions to the forward light-by-light amplitude. An extension of these calculations to physical pion and kaon masses appears promising.

Contents

1	Introduction	2
2	Formalism	4
2.1	Defining a strong isospin-breaking contribution	7
3	Lattice setup	8
4	Connected electromagnetic contribution $a_{\mu,(4)}^{\text{HVP},38}(\Lambda)$	9
4.1	Bare QED two-loop vacuum polarization contribution at fixed Λ from the lattice	10
4.2	The connected contribution $a_{\mu,(4)}^{\text{HVP},38}$ at $m_\pi = m_K \simeq 416$ MeV	12
5	Disconnected electromagnetic contribution $a_{\mu,(2+2)a}^{\text{HVP},38}(\Lambda)$	15
6	Computing the counterterm	16
6.1	The electromagnetic kaon mass splitting	16
6.1.1	Equivalent expressions for the e.m. correction to a hadron mass	17
6.1.2	The elastic contribution	18
6.1.3	Lattice QCD calculation of ΔM_K^{em}	19
6.1.4	Lattice results for ΔM_K^{em}	20
6.1.5	Large Pauli-Villars mass behavior of $\Delta M_K^{em}(\Lambda)$	22
6.2	The response of the kaon mass to an up/down quark mass splitting	24
6.2.1	Lattice results for $\partial\Delta M_K/\partial(m_u - m_d)$ and comparison with chiral perturbation theory	25
6.3	The light-quark mass derivative of the HVP	27
6.3.1	The ratio R_{38K} , and the strong IB contribution in the FLAG24 scheme	29
6.4	The quantity $a_\mu^{\text{HVP},38}(\Lambda)$, continuum extrapolated at fixed Λ	31
6.5	Comparison of lattice results and model estimates	32
7	Conclusion	33
A	Derivation of the expression for the counterterm to $a_\mu^{\text{HVP},38}$	34
B	QED continuum prediction for the connected contribution	35
C	Kaon electromagnetic form factor	36
D	Phenomenological estimate of $a_\mu^{\text{HVP},38}$	38
D.1	The bare electromagnetic contribution at fixed photon cutoff Λ	38
D.2	Low-energy contribution $a_{\mu,em}^{\text{HVP},38,\text{low}}$	40
D.3	Elastic part of the kaon mass splitting	40
D.4	Estimate of R_{38K} and $a_\mu^{\text{HVP},38}$ at the $\text{SU}(3)_f$ point	40

1 Introduction

All charged particles with spin carry an intrinsic magnetic moment, proportional to the spin, with the ‘ g -factor’ as the proportionality constant. The leading prediction for the g -factor from a quantum relativistic description of an elementary charged particle with any spin is $g = 2$. However, further quantum effects modify this value, giving rise to the ‘anomalous magnetic moment’, which for leptons ($\ell = e, \mu, \tau$) is denoted as $a_\ell = (g - 2)/2$. Precise experimental determinations of these quantities have, for a long time, been serving as one of the most stringent tests of the Standard Model (SM) of particle physics.

The level of precision achieved by the direct measurements of a_μ is presently reaching an absolute uncertainty of 22×10^{-11} or 0.19 ppm [1–3]. Achieving this precision on the theory side involves very sophisticated calculations in the SM. Their compilation by a broad consortium of experts has resulted in the ‘Muon $g - 2$ Theory Initiative’ White Papers (WPs) [4, 5]. According to the 2025 WP, the SM prediction for the anomalous magnetic moment of the muon currently has a precision of 62×10^{-11} , and is in good agreement with the experimental world average.

The strong-interaction (hadronic) contributions dominate the theory uncertainty. The leading hadronic contribution, the hadronic vacuum polarisation a_μ^{HVP} illustrated in Fig. 1, carries by itself an absolute uncertainty of 61×10^{-11} . Unlike the first edition of the WP [4], the new edition [5] uses an average of lattice QCD evaluations of the HVP contribution, rather than a dispersive evaluation. The latter are currently being omitted due to strong tensions in the experimental $e^+e^- \rightarrow \pi^+\pi^-$ cross-sections at center-of-mass energies below 1 GeV. Clearly, in order to fully profit from the current precision of the direct measurement of a_μ , and its imminently expected update by the Fermilab collaboration [1], a further factor-of-four reduction in the uncertainty of the HVP contribution is called for, corresponding to a relative error on a_μ^{HVP} at the two-permille level.

It is standard for lattice QCD simulations to be performed with equal up and down quark masses ($m_u = m_d$) and in the absence of photons. However, given the ambitious level of the targeted precision for a_μ^{HVP} , it is imperative to calculate the corrections to the HVP contribution due to the isospin-breaking (IB) effects. The state-of-the-art is to expand the latter in $(m_u - m_d)$ and α to first order. The electromagnetic correction to a_μ^{HVP} is illustrated in Fig. 1. We note that, while the perturbative treatment of isospin-breaking effects has a long tradition [6–8], it was first introduced in lattice QCD in 2013 [9]. Several lattice calculations of these corrections due to IB effects have already been performed [10–16], including one [12] that encompasses all required quark-level diagrams, but the corrections are not yet sufficiently well understood to reduce the theoretical uncertainty on a_μ^{HVP} to the desired level.

The leading correction in α to HVP has a connection to the hadronic light-by-light contribution (HLbL), which is the second-largest hadronic effect in the muon ($g - 2$),

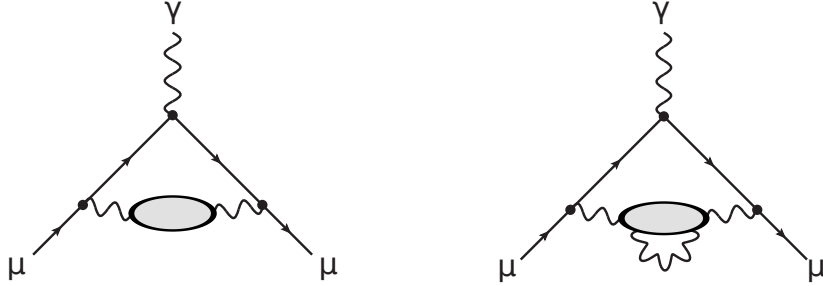


Figure 1: Left: hadronic vacuum polarization contribution to the muon ($g - 2$). Right: electromagnetic correction to the latter. The blobs represents the non-perturbative contribution of QCD degrees of freedom.

recently addressed in the lattice calculations [17–20]. Indeed the $O(\alpha)$ correction to a_μ^{HVP} is expressible in terms of the forward HLbL amplitude [21, 22]. However, while the HLbL contribution is UV-finite, the internal photon leads to divergences in the HVP calculation. To address this issue, we will work in the framework proposed in Ref. [22], where the photon is implemented with a Pauli-Villars regulated propagator, in the continuum and infinite volume. Doing so, one avoids power-law finite-volume effects that arise in the widely used QED_L scheme (see for instance [12, 23, 24]). We will furthermore use the covariant coordinate-space (CCS) representation [25] for obtaining the HVP contribution on the lattice.

Specifically, we calculate the contribution to a_μ^{HVP} of the isospin-violating part $\langle j_\mu^3(x)j_\nu^8(0) \rangle$ of the electromagnetic-current correlator at the $\text{SU}(3)$ -flavour symmetric point for three mass-degenerate quarks: up, down and strange. Clearly, this contribution vanishes in isospin-symmetric QCD¹. The task involves the calculation of the fully connected diagrams at the quark level, for which we also evaluate the (isovector) mass counterterm. This counterterm is fixed by the mass splitting of the kaon, and the combined result is UV finite. Additionally, one needs to include one quark-disconnected diagram, which is already UV-finite. These calculations are performed on five different gauge ensembles generated with $N_f = 3$ dynamical quark flavours by the Coordinated Lattice Simulations (CLS) consortium [26] at a pion and kaon mass around 416 MeV.

We start by defining the basic formalism as well as the different correlation functions to be computed in section 2, following which we present the lattice setup in section 3. The calculation of all relevant contributions is then split in three different sections. At first, we describe how we calculate the fully connected contributions (sec. 4). Here, we also perform a crosscheck, by switching off the gluon interactions and comparing our result to a corresponding continuum calculation for the vacuum polarization contribution in pure QED. In section 5, we compute the quark disconnected contribution, where we also compare our result to the prediction from the pseudoscalar meson exchange. Then in section 6 we determine the counterterm ($m_u - m_d$) by computing the kaon electromagnetic mass splitting

¹The currents j_μ^3 and j_μ^8 correspond to the isovector, respectively isoscalar part of the electromagnetic current.

on the lattice, using again the Pauli-Villars regulated photon propagator. At the end of that section, we gather the three continuum-extrapolated quantities to build the renormalized isospin-violating part of the HVP contribution in the muon ($g - 2$), still at a fixed value of the photon Pauli-Villars cutoff parameters Λ . In a final step, we compare the lattice result extrapolated to $\Lambda = \infty$ with a phenomenological estimate, and conclude in section 7. A number of technical aspects of the lattice calculation and the phenomenological models are provided in appendix.

2 Formalism

To calculate the hadronic vacuum polarization (HVP) contribution to the anomalous magnetic moment of the muon a_μ , we employ the covariant coordinate-space (CCS) method, introduced in Ref. [25]. This method is a proven alternative [27] to the time-momentum representation (TMR) [28], which is the most widely used to calculate this quantity on the lattice. In the CCS method, the HVP contribution is obtained from an integral over the space-time volume ($\int_z \equiv \int d^4z$)

$$a_\mu^{\text{HVP}} = \int_z H_{\lambda\sigma}(z) G_{\lambda\sigma}(z), \quad H_{\lambda\sigma}(z) = -\delta_{\lambda\sigma} \mathcal{H}_1(|z|) + \frac{z_\lambda z_\sigma}{|z|^2} \mathcal{H}_2(|z|), \quad (2.1)$$

where $H_{\lambda\sigma}(z)$ is the CCS kernel and $G_{\lambda\sigma}(z) = \langle j_\lambda^{em}(z) j_\sigma^{em}(0) \rangle_{\text{QCD+QED}}$ is the vector-vector correlator of the electromagnetic vector current

$$j_\lambda^{em}(z) = \frac{2}{3} \bar{u}(z) \gamma_\lambda u(z) - \frac{1}{3} \bar{d}(z) \gamma_\lambda d(z) - \frac{1}{3} \bar{s}(z) \gamma_\lambda s(z). \quad (2.2)$$

In this work, we only consider the contributions of the up, down and strange quarks at the SU(3) flavour symmetric point, $m_u = m_d = m_s$.

Making use of partial integration and exploiting the fact that the electromagnetic current is conserved ($\partial_\lambda j_\lambda(z) = 0$), it is possible to add a total-derivative term $\partial_\lambda [z_\sigma g(|z|)]$ to the CCS kernel, without changing the result for a_μ^{HVP} in the continuum and infinite volume. Besides the transverse ('TV') kernel given in Eq. (2.1), we also define the traceless ('TL') kernel and a variant which is proportional to $z_\lambda z_\sigma$ ('XX') [27, 29]:

$$H_{\lambda\sigma}^{TL}(z) = \left(-\delta_{\lambda\sigma} + 4 \frac{z_\lambda z_\sigma}{|z|^2} \right) \mathcal{H}_2(|z|) \quad (2.3)$$

$$H_{\lambda\sigma}^{XX}(z) = \frac{z_\lambda z_\sigma}{|z|^2} \left(\mathcal{H}_2(|z|) + |z| \frac{d}{d|z|} \mathcal{H}_1(|z|) \right) \quad (2.4)$$

The exact form of the two scalar weight functions \mathcal{H}_1 and \mathcal{H}_2 can be found in [25]. One may also use the rational approximations given in [22]. In case of the disconnected diagram the 'TL' version of the kernel is preferred over the 'XX' one, due to its reduced finite size effects [15]. For that reason all diagrams and values of the connected and disconnected contribution shown in this paper were calculated using the 'TL' kernel if not stated otherwise. But nevertheless in the connected case both versions of the kernel give the same results within error.

In order to generalize the expressions above in terms of the flavour structure, we introduce the isovector (3) and isoscalar (8) parts of the electromagnetic (em) charge matrix,

$$\mathcal{Q}^{(3)} = \begin{pmatrix} 1/2 & 0 & 0 \\ 0 & -1/2 & 0 \\ 0 & 0 & 0 \end{pmatrix}, \quad \mathcal{Q}^{(8)} = \begin{pmatrix} 1/6 & 0 & 0 \\ 0 & 1/6 & 0 \\ 0 & 0 & -1/3 \end{pmatrix}, \quad \mathcal{Q}^{(em)} = \begin{pmatrix} 2/3 & 0 & 0 \\ 0 & -1/3 & 0 \\ 0 & 0 & -1/3 \end{pmatrix}. \quad (2.5)$$

With the quark-flavour triplet $\psi(x) = (u(x), d(x), s(x))^T$, we define the corresponding currents

$$j_\lambda^3(x) = \bar{\psi}^T(x) \gamma_\lambda \mathcal{Q}^{(3)} \psi(x), \quad j_\lambda^8(x) = \bar{\psi}^T(x) \gamma_\lambda \mathcal{Q}^{(8)} \psi(x), \quad (2.6)$$

such that $j_\lambda^{em}(x) = j_\lambda^3(x) + j_\lambda^8(x)$. The correlator $G_{\lambda\sigma}^{ab}(z) = \langle j_\lambda^a(z) j_\sigma^b(0) \rangle_{\text{QCD+QED}}$ then leads to the sub-contributions

$$a_\mu^{\text{HVP},ab} = \int_z H_{\lambda\sigma}(z) G_{\lambda\sigma}^{ab}(z) \quad (2.7)$$

in the anomalous magnetic moment of the muon.

Expanding the correlator to first order in $\alpha = \frac{e^2}{4\pi}$ around the isospin-symmetric QCD, one has

$$\begin{aligned} G_{\lambda\sigma}^{ab}(z) &= \left\langle j_\lambda^a(z) j_\sigma^b(0) \right\rangle_{\text{QCD}} \\ &= -\frac{e^2}{2} \lim_{\Lambda \rightarrow \infty} \left\{ \int_{x,y} \delta_{\nu\rho} [\mathcal{G}(x-y)]_\Lambda \langle j_\lambda^a(z) j_\nu^{em}(y) j_\rho^{em}(x) j_\sigma^b(0) \rangle_{\text{QCD}} + C_T(\Lambda) \right\} \\ &+ O(\alpha^2). \end{aligned} \quad (2.8)$$

The second term is the leading isospin-breaking correction, where we have introduced the Pauli-Villars (PV) regulated photon propagator in Feynman gauge $\delta_{\nu\rho} [\mathcal{G}(x)]_\Lambda$, with [22]

$$[\mathcal{G}(x)]_\Lambda = \frac{1}{4\pi^2|x|^2} - 2G_{\frac{\Lambda}{\sqrt{2}}}(x) + G_\Lambda(x). \quad (2.9)$$

Here, $G_m(x) = mK_1(m|x|)/(4\pi^2|x|)$ stands for the massive scalar propagator, with $K_1(x)$ being the modified Bessel function of the second kind. Fig. 2 compares the photon propagator with its Pauli-Villars-regulated version for various values of the cutoff Λ , often referred to as PV mass. The regulator ensures that the propagator is UV-finite. While UV-finiteness can be achieved already with a single subtraction term, we find that the regularization scheme in Eq. (2.9) reduces cutoff effects more effectively and provides stronger suppression of short-distance contributions.

To obtain a physical result in the limit $\Lambda \rightarrow \infty$, it is necessary to specify an additional renormalization condition complementary to the scale setting procedure in isospin symmetric QCD [30–32]. In this framework, one obtains a counterterm $C_T(\Lambda)$, which is calculated with the same PV regulator (2.9). In Eq. (2.8), the counterterm cancels the UV-divergence that occurs when the vertices in the photon propagator $[\mathcal{G}(x-y)]_\Lambda$ approach each other, $x \rightarrow y$.

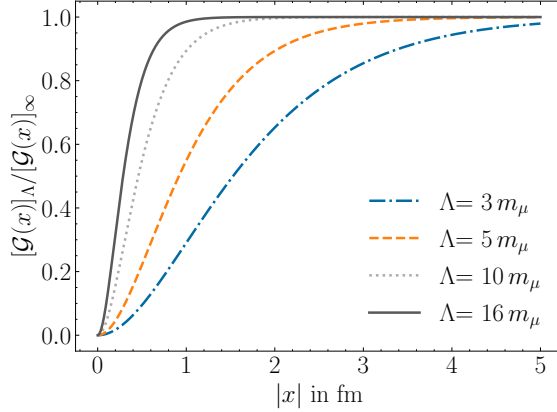


Figure 2: Ratio of the Pauli-Villars-regulated and non-regulated photon propagator for the values of Λ used in later sections.

In the following, we focus on the (3, 8) component of the correlator, $G_{\lambda\sigma}^{3,8}(z)$, for which the leading-order contribution $a_{\mu}^{\text{HVP},38}$ vanishes trivially in isospin-symmetric QCD. We therefore refer to it as the *isospin-violating correlator*. Inserting $G_{\lambda\sigma}^{3,8}(z)$ into Eq. (2.1), we obtain to order $O(\alpha^3)$

$$a_{\mu}^{\text{HVP},38} = \lim_{\Lambda \rightarrow \infty} a_{\mu}^{\text{HVP},38}(\Lambda), \quad a_{\mu}^{\text{HVP},38}(\Lambda) = a_{\mu,em}^{\text{HVP},38}(\Lambda) + C_T(\Lambda), \quad (2.10)$$

$$a_{\mu,em}^{\text{HVP},38}(\Lambda) = -\frac{e^2}{2} \int_{z,x,y} H_{\lambda\sigma}(z) \delta_{\nu\rho} [\mathcal{G}(x-y)]_{\Lambda} \langle j_{\lambda}^3(z) j_{\nu}^{em}(y) j_{\rho}^{em}(x) j_{\sigma}^8(0) \rangle. \quad (2.11)$$

All possible Wick contractions contributing to the four-point function for the isospin-violating correlator in Eq. (2.11) are shown in Fig. 3. In three-flavour theory, due to the property that the sum of the charges of the three light quarks is zero, the diagrams in the bottom row of Fig. 3 vanish at the SU(3)-flavour symmetric point. There, only the diagrams labeled with (4)a, (4)b and (2+2)a contribute. The former are discussed in section 4, while the latter is discussed in section 5.

As a renormalization condition that fully specifies the counterterm, we require the kaon mass splitting $\Delta M_K \equiv M_{K^+} - M_{K^0}$ to assume its physical value $\Delta M_K^{\text{phys}} = -3.934(20)$ MeV [33]. A short derivation, presented in Appendix A, leads then to the following expression for the counterterm,²

$$C_T(\Lambda) = (\Delta M_K^{\text{phys}} - \Delta M_K^{\text{em}}(\Lambda)) R_{38K}, \quad (2.12)$$

$$R_{38K} = \frac{1}{\langle K_0^+ | \bar{u}u - \bar{d}d | K_0^+ \rangle} \left. \frac{\partial a_{\mu}^{\text{HVP},38}}{\partial(m_u - m_d)} \right|_{m_u+m_d, m_s, g_0; \alpha=0} \quad (2.13)$$

$$= \frac{1}{2} \left. \frac{\partial a_{\mu}^{\text{HVP}}}{\partial \Delta M_K} \right|_{\bar{M}_{\pi}, \bar{M}_K, \bar{M}_B}. \quad (2.14)$$

²By default, we use the non-covariant normalization of states, $\langle K_{\mathbf{p}} | K_{\mathbf{p}'} \rangle = (2\pi)^3 \delta^{(3)}(\mathbf{p} - \mathbf{p}')$. Covariantly normalized states will be denoted as $|K_{\mathbf{p}}\rangle$, such that $\langle K_{\mathbf{p}} | K_{\mathbf{p}'} \rangle = (2\pi)^3 2E_{\mathbf{p}} \delta^{(3)}(\mathbf{p} - \mathbf{p}')$.

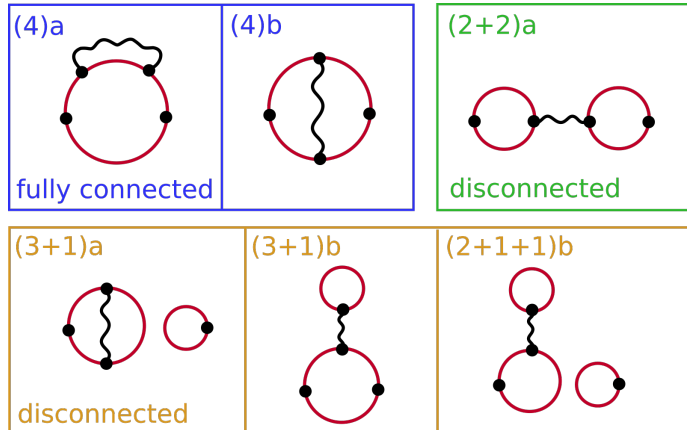


Figure 3: Feynman diagrams depicting all Wick contractions of the four-point function in Eq. (2.11). At the $SU(3)_f$ symmetric point, the diagrams in the lower row vanish.

The quantity $\Delta M_K^{em}(\Lambda)$ is the bare electromagnetic mass splitting, computed with a photon propagator regularized at scale Λ . The factor R_{38K} , as indicated by the second expression,³ expresses the response of the vacuum polarization contribution to the kaon-mass splitting at fixed isospin-averaged⁴ pion, kaon masses and the scale-setting quantity (typically a baryon mass). It has no (leading) scheme dependence and is a renormalization-group-invariant quantity that can be extrapolated to the continuum.

2.1 Defining a strong isospin-breaking contribution

In principle, a lattice computation of $a_\mu^{\text{HVP},38}$ does not require a separation of strong and electromagnetic isospin-breaking effects. However, it can be useful for interpretations in terms of phenomenological calculations based on the Cottingham formula, where $\Delta M_K^{em}(\Lambda)$ is expressed via the kaon forward Compton amplitude. The Compton process is naturally split into the elastic and inelastic contributions and hence we replace $\Delta M_K^{em}(\Lambda)$ in Eq. (2.12) by $(\Delta M_K^{inel}(\Lambda) + \Delta M_K^{elast})$, with the limit $\Lambda \rightarrow \infty$ taken ‘ahead of time’ in ΔM_K^{elast} . Defining

$$a_{\mu,SIB}^{\text{HVP},38} \equiv (\Delta M_K^{phys} - \Delta M_K^{elast}) R_{38K}, \quad (2.15)$$

$$C_T^{inel}(\Lambda) \equiv -\Delta M_K^{inel}(\Lambda) R_{38K}, \quad (2.16)$$

we may then write

$$a_\mu^{\text{HVP},38} = a_{\mu,SIB}^{\text{HVP},38} + \lim_{\Lambda \rightarrow \infty} \left\{ a_{\mu,em}^{\text{HVP},38}(\Lambda) + C_T^{inel}(\Lambda) \right\}, \quad (2.17)$$

such that the first term is interpreted as the strong isospin-breaking contribution and the second one as the electromagnetic contribution. While we do not make use of this separation in our lattice calculation, we use it to organize our phenomenological estimates.

³The factor $\frac{1}{2}$ here accounts for the fact that a_μ^{HVP} contains $a_\mu^{\text{HVP},38}$ and $a_\mu^{\text{HVP},83}$.

⁴The bar over the variables kept constant in Eq. (2.14) indicate that they are isospin-averaged.

One may further isolate an infrared-enhanced set of contributions to $a_{\mu,em}^{\text{HVP},38}(\Lambda)$ that are UV-finite, so that we finally have

$$a_{\mu}^{\text{HVP},38} = a_{\mu,SIB}^{\text{HVP},38} + a_{\mu,em}^{\text{HVP},38,\text{low}} + \lim_{\Lambda \rightarrow \infty} \left\{ a_{\mu,em}^{\text{HVP},38,\text{high}}(\Lambda) + C_T^{\text{inel}}(\Lambda) \right\}. \quad (2.18)$$

The quantity $a_{\mu,em}^{\text{HVP},38,\text{low}}$ will be estimated by using a hadronic model involving the light pseudoscalar mesons of mass below 1 GeV. In doing so, the sum of the Λ -dependent terms in this last equation will be neglected, anticipating that, after the UV-divergence cancels, the remainder is small compared to the first two terms in Eq. (2.18), which are more long-distance dominated. As is well-known, and reviewed below, the (logarithmic) divergence stems from the self-energy of the light quarks, which in the continuum is proportional to the light-quark mass, and therefore has a very small prefactor.

3 Lattice setup

We perform the calculations on a subset of the ensembles generated by the CLS initiative [26, 34], with $O(a)$ improved Wilson-Clover quarks and tree-level $O(a^2)$ improved Lüscher-Weisz gauge action. All our ensembles have degenerate up, down and strange quark masses, corresponding to a pion and kaon mass $m_{\pi} = m_K \sim 416$ MeV, more details are shown in Table 1. To investigate the effect of the finite lattice volume, two of the ensembles have identical simulation parameters, but different volume. One of the ensembles, B450, has periodic boundary conditions in time while the other ones have open boundary conditions.

In order to improve our continuum extrapolations, we use two different discretizations for the vector current, the local (l) and the point-split or conserved (c) discretizations

$$j_{\nu}^l(z) = \bar{q}_z \gamma_{\nu} q_z \quad (3.1)$$

$$j_{\nu}^c(z) = \frac{1}{2} \left[\bar{q}_{z+\hat{\nu}} (\gamma_{\nu} + 1) U_{\nu,z}^{\dagger} q_z + \bar{q}_z (\gamma_{\nu} - 1) U_{\nu,z} q_{z+\hat{\nu}} \right]. \quad (3.2)$$

$U_{\nu,z}$ is the gauge link in the direction ν associated with site z . No further improvements of the vector currents are implemented in this paper.

While the point-split vector currents do not need to be renormalized, a renormalization

Table 1: Parameters of the employed CLS ensembles. The lattice spacing in physical units was extracted from [30]. The pion mass values were taken from [35]. The values for the VMD masses (see Eq. (6.16)) are from [36], and the \hat{Z}_V values from Ref. [37]. All ensembles but B450 have open boundary conditions in time.

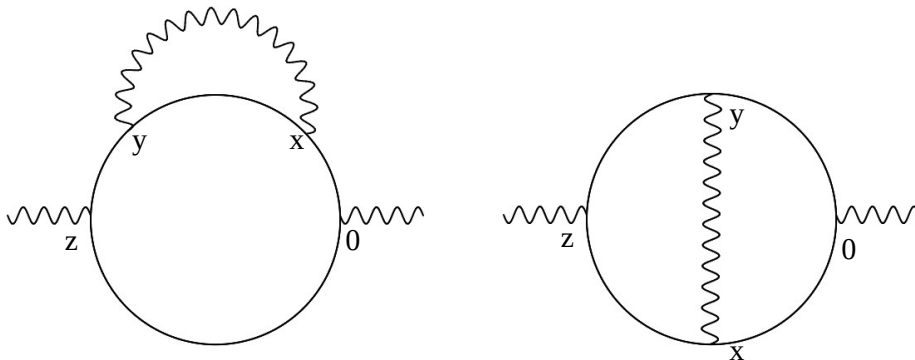
Id	β	$(\frac{L}{a})^3 \times \frac{T}{a}$	a [fm]	m_{π} [MeV]	M_{VMD} [MeV]	$m_{\pi}L$	L[fm]	\hat{Z}_V
H101	3.4	$32^3 \times 96$	0.08636	416(4)	921(13)	5.8	2.8	0.71540
B450	3.46	$32^3 \times 64$	0.07634	415(4)	942(25)	5.1	2.4	0.72645
H200	3.55	$32^3 \times 96$	0.06426	416(5)	979(26)	4.3	2.1	0.74030
N202		$48^3 \times 128$		412(5)	952(15)	6.4	3.1	
N300	3.7	$48^3 \times 128$	0.04981	419(4)	1001(23)	5.1	2.4	0.75912

Table 2: The number of used configurations for every ensemble and each part of the calculation.

Part	H101	B450	H200	N202	N300
Connected	200	200	200	120	120
Disconnected	182	200	200	200	200
Kaon mass splitting	200	200	200	200	200
Kaon mass derivative	200	200	200	200	200
HVP derivative	2000	1600	2000	899	1540

factor \hat{Z}_V is required for the local currents. The renormalized local vector current is obtained from $j_\nu^{l,\text{ren}}(z) = \hat{Z}_V j_\nu^l(z)$. We absorb the combined renormalization factors for each local vector current in a global multiplicative constant. This constant always corresponds to \hat{Z}_V raised to the power of the number of local vector currents n_l : $\mathcal{Z} = \hat{Z}_V^{n_l}$. We extracted \hat{Z}_V for each value of β from Ref. [37]; the values are collected in Table 1. Apart from vector currents, pseudoscalar densities also appear in the course of our calculations, but their renormalization factors cancel and are therefore not needed. Finally, we provide the level of statistics collected on each gauge ensemble for the different key observables in Table 2.

4 Connected electromagnetic contribution $a_{\mu,(4)}^{\text{HVP},38}(\Lambda)$



(a) Diagram (4)a: the self-energy diagram, which contributes twice.

(b) Diagram (4)b: the genuine 2-loop diagram.

Figure 4: The fully connected diagrams which need to be calculated for $a_{\mu,(4)}^{\text{HVP},38}$.

In this section, we describe the calculation of the connected contribution. Using Wick's theorem for the four-point function in Eq. (2.11) results in three different fully connected quark contractions, just as in the case of the calculation of the hadronic light-by-light contribution [36]. Two of these diagrams result in the same contribution. They correspond to the case depicted in Fig 4a, where the photon propagator can either be on the upper or

the lower quark propagator. We refer to this diagram as the *self-energy* (SE) part,

$$C_{\rho\nu\lambda\sigma}^{SE}(x, y, z) = -2 \text{Re}\langle \text{Tr}[S(0, x)\gamma_\rho S(x, y)\gamma_\nu S(y, z)\gamma_\lambda S(z, 0)\gamma_\sigma] \rangle_U. \quad (4.1)$$

Additionally, one needs to calculate the *genuine 2-loop* (2L) part

$$C_{\rho\nu\lambda\sigma}^{2L}(x, y, z) = -2 \text{Re}\langle \text{Tr}[S(0, y)\gamma_\nu S(y, z)\gamma_\lambda S(z, x)\gamma_\rho S(x, 0)\gamma_\sigma] \rangle_U. \quad (4.2)$$

The trace needs to be taken with respect to the Dirac and color indices, while $\langle \dots \rangle_U$ denotes the expectation value over gauge configurations and $S(x, y)$ is the quark propagator where the sink is at x and the source is at y . In total the connected contribution yields

$$a_{\mu, (4)}^{\text{HVP}, 38}(\Lambda) = -f_Q^{(4)} \mathcal{Z} \frac{e^2}{2} \int_{z, x, y} H_{\lambda\sigma}(z) \delta_{\nu\rho} [\mathcal{G}(x - y)]_\Lambda \quad (4.3)$$

$$(2 C_{\rho\nu\lambda\sigma}^{SE}(x, y, z) + C_{\rho\nu\lambda\sigma}^{2L}(x, y, z)).$$

where the factor ‘2’ for the SE part is due to the two possible positions of the photon propagator. The charge factor $f_Q^{(4)}$ for the connected contribution is given by the trace over the product of charge matrices $f_Q^{(4)} = \text{Tr}\{\mathcal{Q}^{(3)}\mathcal{Q}^{(em)}\mathcal{Q}^{(em)}\mathcal{Q}^{(8)}\} = \frac{1}{36}$, using Eq. (2.5).

For the implementation of Eq. (4.3) in our lattice calculation, we perform the summation over the x and z vertex on the fly for fixed values of y . Specifically, Eq. (4.3) is rewritten as

$$a_{\mu, (4)}^{\text{HVP}, 38}(\Lambda) = -f_Q^{(4)} \mathcal{Z} \pi^2 e^2 a^8 \int_0^\infty d|y| |y|^3 \sum_{z, x} H_{\lambda\sigma}(z) \delta_{\nu\rho} [\mathcal{G}(x - y)]_\Lambda \quad (4.4)$$

$$(2 C_{\rho\nu\lambda\sigma}^{SE}(x, y, z) + C_{\rho\nu\lambda\sigma}^{2L}(x, y, z)).$$

The integrand of Eq. (4.4) is calculated on the lattice for different values of y along the (1, 1, 1, 1) direction. The integral over $|y|$ is then computed using the trapezoidal rule. The origin was assigned to the middle time slice of each lattice. For the calculation of C^{SE} , it is sufficient to use two one-to-all propagators with their origins at the y and 0 vertices. For C^{2L} , we additionally make use of a sequential propagator starting at the 0 vertex, going over the x vertex and ending at the z vertex.

As mentioned in the previous section, we use both local and conserved discretizations of the vector currents. This applies only to the vertices over which the sum is performed, i.e. the x and z vertices. The discretization scheme is denoted as XdZd, where the character ‘d’ is replaced with ‘l’ for a local current or ‘c’ for a conserved current at the corresponding vertex.

4.1 Bare QED two-loop vacuum polarization contribution at fixed Λ from the lattice

In order to test whether the proposed methodology is viable, we first perform the calculation of $a_{\mu, (4)}^{\text{HVP}, 38}(\Lambda)$ on ensembles without the strong interaction, i.e. where the gauge field variables $U \in \text{SU}(3)_c$ are set to unity on all lattice links. Owing to the use of the Pauli-Villars regulated photon propagator (as opposed to the regularization by the finite

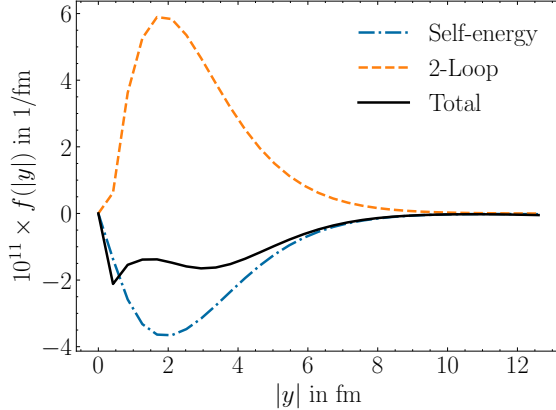


Figure 5: The integrand of Eq. (4.4) for the self-energy (blue) and 2-loop (orange) part separately as well as combined to the total (black), given by $2 \times \text{SE} + 2\text{L}$. It is shown on the gluonless ensemble with $L = 64$ with the XcZc discretization and the ‘TL’ kernel. The lepton in the loop has mass $m_\ell = m_\mu$ and the Pauli-Villars mass is set to $\Lambda = 3 m_\mu$.

Table 3: Parameters of the gluonless ensembles. For each lattice the time extend is the same as L , i.e. they have a volume of L^4 .

L	24	32	40	48	56	64	72	80
am_μ	0.3	0.225	0.18	0.15	0.13	0.1125	0.1	0.09

lattice spacing), we can directly compare the lattice results to continuum calculations (see Appendix B). This serves as a useful crosscheck for our methodology.

To this end, we employ eight L^4 lattices with different spacings, but with a constant volume of $m_\mu L = 7.2$, with parameters provided in Table 3. We set the lepton mass m_ℓ appearing in the loop to be equal to the muon mass, $m_\ell = m_\mu$, while the Pauli-Villars mass of the photon is set to $\Lambda = 3 m_\mu$ for the purpose of this test. An example of the integrand of Eq. (4.4) in the case of the lattice with $L = 64$ is shown in Fig. 5. In this example, the currents at both the x and z vertices are conserved, and the ‘TL’ version of the CCS kernel is used.

The results for each ensemble using the four different discretizations are shown in Fig. 6. We perform a continuum extrapolation by fitting the data points with the function

$$f_{fit}(a) = c_0 + c_1 a + c_2 a^2 + c_3 a^3. \quad (4.5)$$

Of special interest is the extrapolation of the total quantity in Fig. 6c. For both cases where the current at the x vertex is conserved the extrapolation is flat without much curvature. Based on this observation the XcZl and XcZc discretization schemes are the ones used in the QCD calculation later on. This plot also shows the value resulting from the previously mentioned continuum prediction (see Appendix B) as a black triangle. This value was obtained completely independently from the calculations described here and lies where all of the lines of the different discretizations meet. The results of the continuum extrapolation of the individual diagrams for different discretizations are given in Table 4.

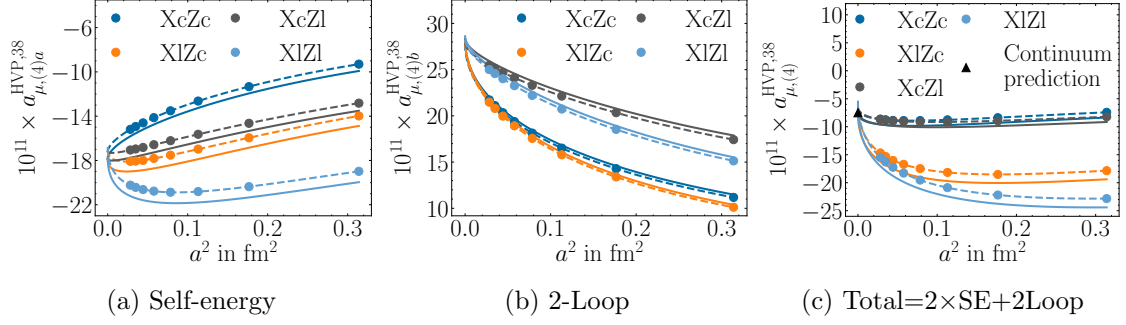


Figure 6: Continuum extrapolation of the self-energy and 2-loop parts and the total value for the ‘gluonless’ lattices and $\Lambda = 3 m_\mu$. The different colors represent the different discretizations used for the current at the x and z vertices. Additionally, fits of the form given by Eq. (4.5) are shown. The dashed lines correspond to fits performed directly on the data points, while the solid lines represent the volume-corrected fits. The volume correction was calculated by doubling the volume of the coarsest lattices and adding the difference to the fit function. The figure showing the total result also includes the continuum prediction indicated by a black triangle, which was computed following the methodology outlined in Appendix B.

Table 4: Results of the volume corrected continuum extrapolations in Fig. 6. The values are given in units of 10^{-11} . The errors are from the fit. The expected value of the total result is -7.499×10^{-11} , as obtained using the methodology outlined in appendix B.

	XlZl	XcZl	XlZc	XcZc
Total	-6.90(15)	-7.36(16)	-7.44(18)	-7.56(18)
2-Loop	28.62(11)	28.32(8)	28.42(9)	28.18(7)
Self-Energy	-17.76(11)	-17.84(11)	-17.93(13)	-17.87(12)

The discretization for which both the currents at the x and z vertices are conserved yields a result especially close to the value from the continuum prediction.

4.2 The connected contribution $a_{\mu,(4)}^{\text{HVP},38}$ at $m_\pi = m_K \simeq 416 \text{ MeV}$

The successful crosscheck on the ‘gluonless’ ensembles against the continuum calculation confirmed the viability of the methodology. Now, the same principles shall be used for the calculation on the ensembles introduced in section 3. The integrands of the different parts on the N300 ensemble can be seen in Fig. 7. For these plots the XcZl discretization and a Pauli-Villars mass of $5 m_\mu$ is used. While the ‘gluonless’ calculation seen in Fig. 5 already showed a cancellation between the self-energy and 2-loop part, the cancellation is much more severe for the QCD calculation. The combined integrand in Fig. 7b is much smaller than the individual contributions from the self-energy and 2-loop diagrams depicted in Fig. 7a. This worsens the signal-to-noise ration of the total result compared to the contributions of the individual diagrams with the former being consistent with 0

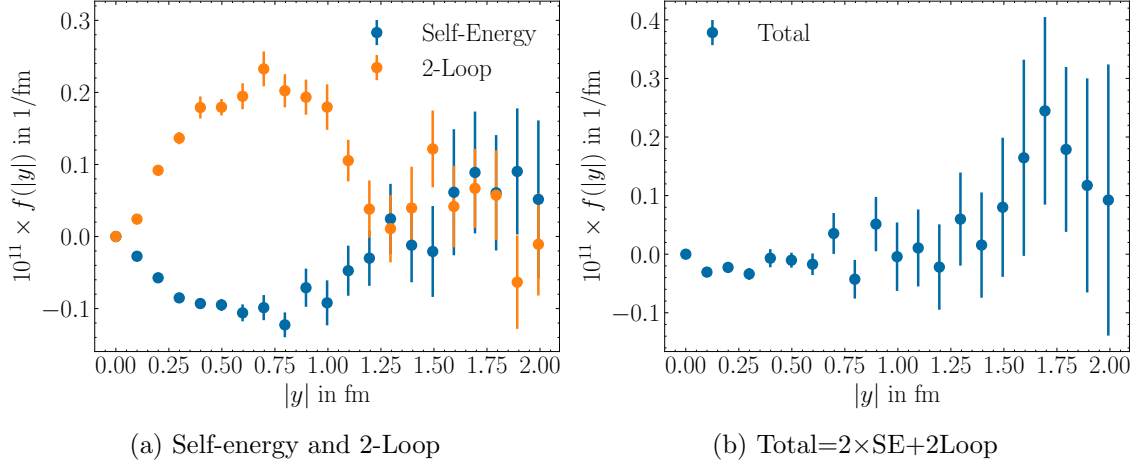


Figure 7: The integrand of Eq. (4.4) for the self-energy and 2-loop part separately on the left side as well as combined on the right side. It is shown on the N300 ensemble with the XcZl discretization and the ‘TL’ kernel. The Pauli-Villars mass is set to $\Lambda = 5 m_\mu$.

starting at around $|y| = 1$ fm. This behavior is seen for all ensembles, discretizations and CCS kernels we investigated.

Based on this observation, the integrand in Eq. (4.4) is only evaluated up to a cut in $|y|$, which was chosen for each ensemble individually. For N300 this value is $|y| = 1.45$ fm. Another interesting observation is that the values of the integrands are more than an order of magnitude smaller than in the QED case and also much more short ranged, even before the cancellation between the self-energy and 2-loop part happens. This means one can also expect a much smaller value for the continuum extrapolated result.

This continuum extrapolation of the different parts for a Pauli-Villars mass of $16 m_\mu$ can be seen in Fig. 8. The fit function used in this case was modified compared to the ‘gluonless’ case, because there are now several lattice volumes involved and fewer data points overall,

$$f_{fit}(a, m_\pi L) = c_0 + c_1 a^2 + c_2 e^{-\frac{m_\pi L}{2}}. \quad (4.6)$$

The expectation set by the plots of Fig. 7 holds true: while we clearly observe a signal for the self-energy part and the two-loop part, a vast cancellation leads to the total contribution vanishing within its uncertainty. Another interesting observation from these plots is the behavior of the finite volume correction. For the two parts separately the volume correction is important, but when added together it is not statistically significant.

We finish this section by looking at the dependence on the PV-mass of the total connected contribution. Table 5 lists the four calculated values together with their uncertainty and Fig. 9 shows their dependence on Λ . The values grow more negative for larger Λ values, but the errors increase approximately at the same rate. This results in all values being consistent with zero within uncertainties, as previously noted.

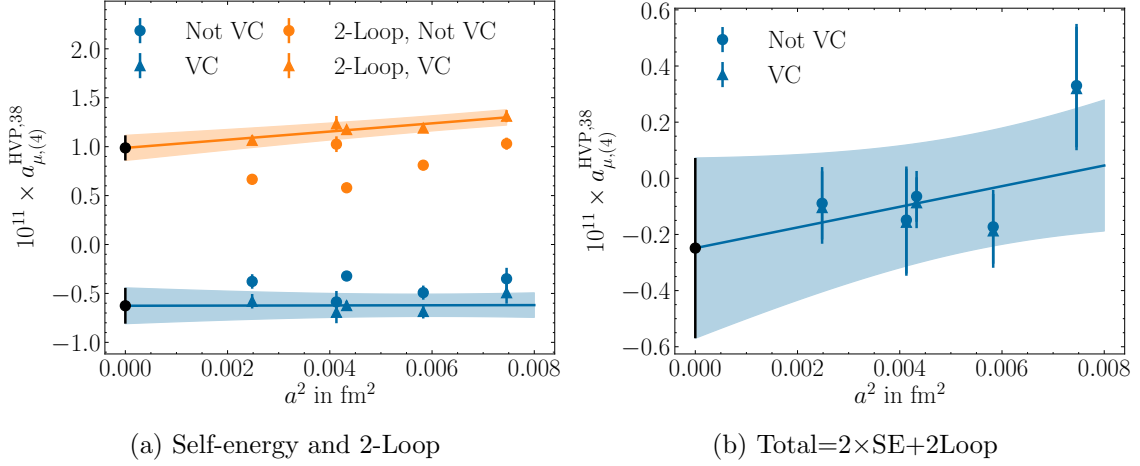


Figure 8: Continuum extrapolation of the self-energy and 2-loop parts on the left side as well as the total value on the right side for the QCD ensembles. The Pauli-Villars mass is set to $\Lambda = 16 m_\mu$. H200 is shown with a slight offset to higher a^2 to make it distinguishable from N202. Eq. (4.6) is used as an ansatz for the fit function. The dots are the results from each ensemble, while the triangles are the same results, but with the volume term of the fit function subtracted without adjusting the error bars. The straight lines are the fits to these volume-corrected points. The black dots are the results of the continuum extrapolation.

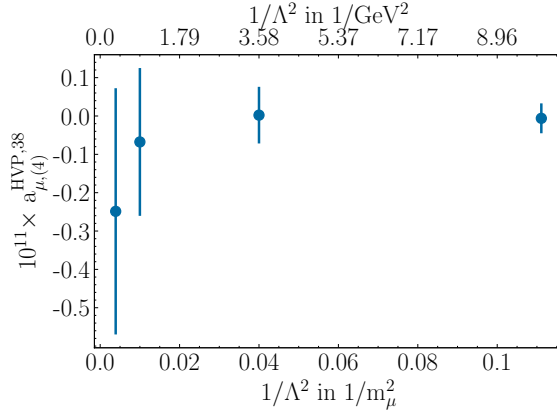


Figure 9: Dependence on Λ for the connected contribution. The coordinates of the data points are collected in Table 5.

Table 5: Continuum extrapolated values of $a_{\mu,(4)}^{\text{HVP},38}$ for the different PV-mass values.

Λ/m_μ	3	5	10	16
m_μ^2/Λ^2	0.11	0.04	0.01	0.004
$10^{11} \times a_{\mu,(4)}^{\text{HVP},38}(\Lambda)$	-0.006(39)	0.002(74)	-0.068(193)	-0.249(321)

5 Disconnected electromagnetic contribution $a_{\mu,(2+2)a}^{\text{HVP},38}(\Lambda)$

In addition to the fully connected diagrams shown in Fig. 4, there is also one disconnected diagram contributing to $a_{\mu}^{\text{HVP},38}$ in Eq. (2.11) at the $\text{SU}(3)_f$ symmetric point, which in the nomenclature of Ref. [14] is referred to as $(2+2)a$. This diagram is characterized by two disconnected valence quark loops that are connected by the photon propagator,

$$a_{\mu,(2+2)a}^{\text{HVP},38}(\Lambda) = -e^2 f_{\mathcal{Q}}^{(2+2)a} \mathcal{Z} \int_{z,x,y} H_{\lambda\sigma}(z) \delta_{\nu\rho} [\mathcal{G}(x-y)]_{\Lambda} \left\langle \hat{\Pi}_{\lambda\nu}(z,x) \hat{\Pi}_{\rho\sigma}(y,0) \right\rangle_U. \quad (5.1)$$

The two-point correlation function using local vector currents is given by

$$\Pi_{\mu\nu}(x,y) = -\text{Re} \left(\text{Tr} \left[S(y,x) \gamma_{\mu} S(x,y) \gamma_{\nu} \right] \right). \quad (5.2)$$

The vacuum expectation value needs to be subtracted in order to avoid double counting of the contribution, where the two QCD ‘blobs’ are not interconnected,

$$\hat{\Pi}_{\mu\nu}(x,y) = \Pi_{\mu\nu}(x,y) - \langle \Pi_{\mu\nu}(x,y) \rangle_U. \quad (5.3)$$

The charge factor for the ‘38’ contribution is obtained from

$$f_{\mathcal{Q}}^{(2+2)a} = \text{Tr} \{ \mathcal{Q}^{(3)} \mathcal{Q}^{(em)} \} \text{Tr} \{ \mathcal{Q}^{(em)} \mathcal{Q}^{(8)} \} = \frac{1}{12}. \quad (5.4)$$

A recent lattice QCD calculation of this contribution [15] shows a significant contribution to the HVP from this particular diagram at the physical point. Here, we use the results from Ref. [15] for the ensembles at the $\text{SU}(3)_f$ symmetric point normalized to the correct charge factor for the ‘38’ contribution. Since the $(2+2)a$ contribution is UV-finite [15], the Pauli-Villars mass Λ is taken to be infinite in Eq. (5.1).

A phenomenological description of the $(2+2)a$ contribution in terms of the exchange of neutral pseudoscalar mesons π^0 , η , η' and the charged pion loop was also discussed in Ref. [15]. An important difference between the calculation at the physical point and the $\text{SU}(3)_f$ symmetric point is the relative size of the charged pion loop and the pseudoscalar meson exchange (PME) contribution. While the former is dominant at the physical point, the hierarchy is swapped at the $\text{SU}(3)_f$ symmetric point. In Fig 10a, the integrand with respect to $|y|$ of the Eq. (5.1) is shown after performing the integration over x and z . We observe good agreement between the prediction from the pseudoscalar mesons and the lattice data. However, following the procedure from Ref. [15], we also fit the contribution of the charged pion loop to the lattice data to approximate the tail of the integrand for $|y| > L/2$ by the total prediction from the model. From Fig. 10a, one can see that the tail is totally dominated by the PME contribution, a fact that does not hold anymore when approaching the physical pion mass.

In order to remove the cut-off effects, we perform a simple continuum extrapolation for the results of the $(2+2)a$ contribution with a fit linear in a^2 . The fit is depicted in Fig. 10b. The continuum result for this contribution to the isospin-violating part of the HVP reads

$$a_{\mu,(2+2)a}^{\text{HVP},38} = -0.53(17) \times 10^{-11}. \quad (5.5)$$

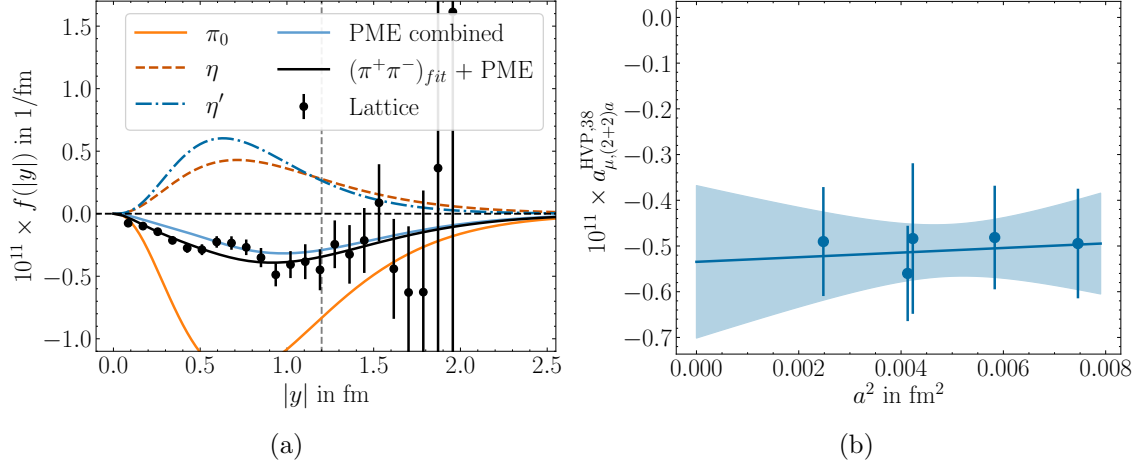


Figure 10: (a) Integrand of Eq. (5.1) with respect to $|y|$ following the procedure in Ref. [15], together with the prediction from the pseudoscalar mesons. The solid light blue curve is the sum of the contributions from π^0 , η and η' . For the black curve the charged pion contribution is fitted to the lattice data. The vertical dashed line represents the cut in $|y|$ from which we use the model to approximate the tail of the integrand. (b) Continuum extrapolation of the results computed on the ensembles from Table 1. H200 is shown with a slight offset to higher a^2 to make it distinguishable from N202.

6 Computing the counterterm

In order to obtain the counterterm according to Eq. (2.12), we split the calculation into three different parts. These are the electromagnetic kaon mass splitting, the light-quark mass derivative of the kaon mass and the light-quark mass derivative of the leading-order HVP. We discuss the calculation of the three quantities in that order.

6.1 The electromagnetic kaon mass splitting

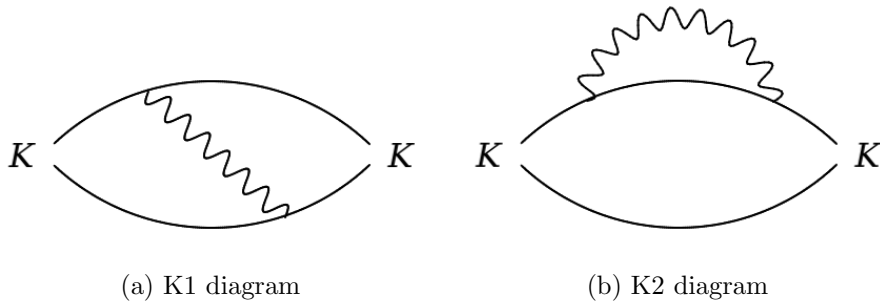


Figure 11: The Feynman diagrams of the leading order contributions to the e.m. mass splitting of the kaon. The bottom quark line corresponds to the strange quark. At the $SU(3)_f$ symmetric point, only these two diagrams contribute to the mass splitting.

The first quantity that needs to be calculated for the counterterm is the leading electromagnetic contribution to the charged-neutral kaon mass splitting. From this point on, it will be abbreviated as the e.m. kaon mass splitting. At the $SU(3)_f$ symmetric point, only the two diagrams in Fig. 11 contribute to the e.m. mass splitting; see for instance Ref. [9]. These two diagrams can be interpreted as the self energy correction to the kaon mass.

For large separation times between the two photon vertices, only intermediate kaon states contribute to this correction [38], in other words, the elastic contribution dominates; the latter can be calculated analytically (see below). This naturally leads to the strategy of using the lattice calculation up to a maximum time separation between the two currents, while beyond that, we use the aforementioned analytic expression, directly in the continuum and with infinite volume [22]. This procedure avoids power-law finite-size effects, which would otherwise affect the four-point function at large separation times [38].

In this section, we first discuss the calculation of the elastic part. Then the lattice calculation, which also includes the inelastic part, will be presented. Following that, we apply the Operator Product Expansion to predict the behavior of the e.m. kaon mass splitting at large PV masses. Finally, we compare this prediction to our results.

6.1.1 Equivalent expressions for the e.m. correction to a hadron mass

In the following, we review various equivalent expressions for the e.m. correction to a hadron mass. We start by considering the leading-order electromagnetic corrections to the two-point function of a general hadron

$$C_2(z_0) = \langle \bar{h}(z_0)h(0)^\dagger \rangle_{\text{QCD+QED}} = C_2^{(0)}(z_0) + C_2^{(2)}(z_0) + O(\alpha^2), \quad (6.1)$$

$$C_2^{(0)}(z_0) = \langle \bar{h}(z_0)h(0)^\dagger \rangle_{\text{QCD}}, \quad (6.2)$$

$$C_2^{(2)}(z_0) = -\frac{e^2}{2} \int_{x,y} \delta_{\nu\rho} [\mathcal{G}(x-y)]_\Lambda \langle \bar{h}(z_0)j_\rho^{em}(x)j_\nu^{em}(y)h(0)^\dagger \rangle_{\text{QCD}}. \quad (6.3)$$

In these equations $\bar{h}(z_0) = \int d^3z h(z)$ is the interpolator for a hadron at rest. The mass of the hadron can be extracted from this using the usual approach

$$\begin{aligned} M_h &= -\lim_{z_0 \rightarrow \infty} \frac{d}{dz_0} \log C_2(z_0) = -\lim_{z_0 \rightarrow \infty} \frac{d}{dz_0} \log \left(C_2^{(0)}(z_0) + C_2^{(2)}(z_0) \right) \\ &= -\lim_{z_0 \rightarrow \infty} \frac{d}{dz_0} \left(\log \left(C_2^{(0)}(z_0) \right) + \frac{C_2^{(2)}(z_0)}{C_2^{(0)}(z_0)} \right) + \dots = M_h^{(0)} + \delta M_h. \end{aligned} \quad (6.4)$$

We are interested in the correction to the hadron mass δM_h , for which we now have the expression

$$\delta M_h = \frac{e^2}{2} \lim_{z_0 \rightarrow \infty} \frac{d}{dz_0} \frac{\int_{x,y} \delta_{\nu\rho} [\mathcal{G}(x-y)]_\Lambda \langle \bar{h}(z_0)j_\rho^{em}(x)j_\nu^{em}(y)h(0)^\dagger \rangle}{\langle \bar{h}(z_0)h(0)^\dagger \rangle}. \quad (6.5)$$

This formula corresponds to the use of the ‘summation method’ [39] to extract the ground-state matrix element. By using the fact that only the relative position of the two vector

currents to one another as well as their relative position to the hadron interpolators is of importance, we can rewrite the upper integrals in the following way:

$$\begin{aligned} & \int_{x,y} \delta_{\nu\rho} [\mathcal{G}(x-y)]_{\Lambda} \langle \bar{h}(z_0) j_{\rho}^{em}(x) j_{\nu}^{em}(y) h(0)^{\dagger} \rangle \\ &= \int_{-\infty}^{\infty} dy_0 \left\langle \bar{h} \left(\frac{z_0}{2} \right) \left(\int_x \delta_{\nu\rho} [\mathcal{G}(x)]_{\Lambda} j_{\rho}^{em}(x+y_0\hat{e}_0) j_{\nu}^{em}(y_0\hat{e}_0) \right) \bar{h} \left(-\frac{z_0}{2} \right)^{\dagger} \right\rangle. \end{aligned} \quad (6.6)$$

For very large z_0 only the ground state of the hadron contributes to the four-point function. At that point there is translational invariance for an operator insertion between the \bar{h}^{\dagger} and the \bar{h} operator, which means the integral over y_0 simply yields a factor of z_0 , and we can write

$$\delta M_h = \frac{e^2}{2} \lim_{z_0 \rightarrow \infty} \frac{\int_x \delta_{\nu\rho} [\mathcal{G}(x)]_{\Lambda} \langle \bar{h}(\frac{z_0}{2}) j_{\rho}^{em}(x) j_{\nu}^{em}(0) \bar{h}(-\frac{z_0}{2})^{\dagger} \rangle}{\langle \bar{h}(\frac{z_0}{2}) \bar{h}(-\frac{z_0}{2})^{\dagger} \rangle}. \quad (6.7)$$

This expression corresponds to the ‘mid-point’ method used in hadron structure calculations for extracting the ground-state matrix element. We now introduce

$$\begin{aligned} f_{z_0}(x_0) &= \frac{e^2}{2} \frac{\int d^3x \delta_{\nu\rho} [\mathcal{G}(x)]_{\Lambda} \langle \bar{h}(z_0) j_{\rho}^{em}(x) j_{\nu}^{em}(0) \bar{h}(-z_0)^{\dagger} \rangle}{\langle \bar{h}(z_0) \bar{h}(-z_0)^{\dagger} \rangle} \\ \xrightarrow{z_0 \rightarrow \infty} f(x_0) &= \frac{e^2}{2} \int d^3x \delta_{\nu\rho} [\mathcal{G}(x)]_{\Lambda} \langle h_{\mathbf{p}=0} | T \{ j_{\rho}^{em}(x) j_{\nu}^{em}(0) \} | h_{\mathbf{p}=0} \rangle, \end{aligned} \quad (6.8)$$

where we dropped the factor $1/2$ of z_0 in the first definition since it does not matter in the limit. This finally leaves us with

$$\delta M_h = \int_{-\infty}^{\infty} dx_0 f(x_0), \quad (6.9)$$

which is the form typically used in continuum field-theoretic treatments.

6.1.2 The elastic contribution

We now shift our attention from a general hadron to the kaon. Introducing the relativistically normalized kaon states, indicated by bold symbols,

$$\langle \mathbf{K}_q | \mathbf{K}_p \rangle = 2E_q L^3 \delta_{qp}. \quad (6.10)$$

we find an expression for the elastic contribution to the integrand $f(x_0)$ by inserting a complete set of one-particle states,

$$f_{elast}(x_0) \stackrel{x_0 \geq 0}{=} \frac{e^2}{2} \int d^3x \delta_{\nu\rho} [\mathcal{G}(x)]_{\Lambda} \frac{1}{L^3} \sum_{\mathbf{p}} \frac{1}{4E_{\mathbf{p}} M_K} \langle \mathbf{K}_0 | j_{\rho}^{em}(x) | \mathbf{K}_{\mathbf{p}} \rangle \langle \mathbf{K}_{\mathbf{p}} | j_{\nu}^{em}(0) | \mathbf{K}_0 \rangle. \quad (6.11)$$

Because of translational invariance, the matrix elements can be rewritten as

$$\begin{aligned} \langle \mathbf{K}_0 | j_{\rho}^{em}(x) | \mathbf{K}_{\mathbf{p}} \rangle &= \langle \mathbf{K}_0 | e^{Hx_0 - i\mathbf{p}\cdot\mathbf{x}} j_{\rho}^{em}(0) e^{-Hx_0 + i\mathbf{p}\cdot\mathbf{x}} | \mathbf{K}_{\mathbf{p}} \rangle \\ &= \langle \mathbf{K}_0 | j_{\rho}^{em}(0) | \mathbf{K}_{\mathbf{p}} \rangle e^{(M_k - E_{\mathbf{p}})x_0 + i\mathbf{p}\cdot\mathbf{x}}. \end{aligned} \quad (6.12)$$

In Euclidean space, the matrix element from the right-hand side of the last equation is connected to the form factor $F(-Q^2)$ by

$$\langle \mathbf{K}_{\mathbf{p}} | j_{\rho}^{em}(0) | \mathbf{K}_{\mathbf{k}} \rangle = -i(P_{\rho} + K_{\rho})F(-(P - K)^2) \quad (6.13)$$

with the Euclidean on-shell four-momentum vectors $P = (iE_{\mathbf{p}}, \mathbf{p})$ and $K = (iE_{\mathbf{k}}, \mathbf{k})$. Substituting Eqs. (6.12) and (6.13) into (6.11) yields the following result for the elastic integrand, now valid for all values of x_0 :

$$f_{elast}(x_0) = \frac{e^2}{4L^3} \int d^3x [\mathcal{G}(x)]_{\Lambda} \sum_{\mathbf{p}} e^{(M_{\mathbf{k}} - E_{\mathbf{p}})|x_0| + i\mathbf{p} \cdot \mathbf{x}} \frac{E_{\mathbf{p}} + M_K}{E_{\mathbf{p}}} F^2(-(P - K)^2). \quad (6.14)$$

In the limit of infinite volume, the expression simplifies to

$$f_{elast}(x_0) = \frac{e^2}{8\pi^2} \int_0^{\infty} dp p^2 e^{(M_{\mathbf{k}} - E_{\mathbf{p}})|x_0|} \frac{E_{\mathbf{p}} + M_K}{E_{\mathbf{p}}} F^2(-(P - K)^2) \times \quad (6.15)$$

$$\times \left[\frac{e^{-|\mathbf{p}||x_0|}}{2|\mathbf{p}|} - \frac{e^{-\sqrt{|\mathbf{p}|^2 + \Lambda^2/2}|x_0|}}{\sqrt{|\mathbf{p}|^2 + \Lambda^2/2}} + \frac{e^{-\sqrt{|\mathbf{p}|^2 + \Lambda^2}|x_0|}}{2\sqrt{|\mathbf{p}|^2 + \Lambda^2}} \right].$$

It is important to note that the derivation above refers to the rest frame of the kaon, i.e. $K = (iM_K, \mathbf{0})$ in these equations. We also remark that $\int_{-\infty}^{\infty} dx_0 f_{elast}(x_0)$ yields an expression for ΔM_K^{elast} similar but not identical to the one obtained in [40], where the ‘elastic contribution’ is defined via the forward Compton amplitude. The two expressions do however agree in the limit where the argument of the form factor is small.

The vector meson dominance (VMD) form factor

$$F_{\text{VMD}}(-Q^2) = \frac{1}{1 + Q^2/M_{\text{VMD}}^2} \quad (6.16)$$

will be used to evaluate Eq. (6.15). This turned out to be sufficient for describing the data, and appendix C provides a more detailed discussion regarding the form factor. The VMD mass values for the different ensembles are collected in Table 1.

6.1.3 Lattice QCD calculation of ΔM_K^{em}

For the total contribution there are three parts which have to be evaluated on the lattice. Writing them in terms of propagators yields:

$$C^{2pt}(x, y) = -\text{Re}\langle \text{Tr}[S^l(y, x)\gamma_5 S^s(x, y)\gamma_5] \rangle_U, \quad (6.17)$$

$$C_{\nu\rho}^{K1}(x, y, z) = -2 \text{Re}\langle \text{Tr}[S^l(y, z)\gamma_{\nu} S^l(z, x)\gamma_5 S^s(x, 0)\gamma_{\rho} S^s(0, y)\gamma_5] \rangle_U, \quad (6.18)$$

$$C_{\nu\rho}^{K2}(x, y, z) = -2 \text{Re}\langle \text{Tr}[S^l(y, 0)\gamma_{\rho} S^l(0, z)\gamma_{\nu} S^l(z, x)\gamma_5 S^s(x, y)\gamma_5] \rangle_U. \quad (6.19)$$

$S^s(x, y)$ and $S^l(x, y)$ are now specifically the strange and light-quark propagators, respectively, with their source at y and sink at x . The two four-point functions represent the Feynman diagrams shown in Fig. 11, while the two-point function represents the propagation of a kaon. For these diagrams we use sequential as well as doubly sequential propagators. This is because we cannot use the same trick as in the case of the connected

contribution in section 4, were we used rotational invariance to reduce one of the integrals over the vertices to an integral over just the absolute distance of this vertex to the origin. For the K1 diagram, we start with a one-to-all propagator from the origin and calculate two sequential propagators over the x and y vertices respectively. On the other hand, for the K2 diagram a double sequential propagator, which starts at the 0 vertex and goes over the x and y vertices, is needed.

As with the elastic contribution, we have to project the kaon to zero momentum, which means both x and y are restricted to a single time slice with $x_0 = -t_s/2$ and $y_0 = t_s/2$, and t_s is the separation time between the creation and annihilation operators of the kaon. In terms of the diagrams defined above, making use of the property $\text{Tr } \mathcal{Q}^{(em)} = 0$, we can write down the e.m. kaon mass splitting in the following way,

$$\Delta M_K^{em}(\Lambda) = \lim_{t_s \rightarrow \infty} \frac{e^2 f_{\mathcal{Q}}^{\Delta M_K^{em}}}{2} a^4 \sum_{z_0=-\infty}^{\infty} \frac{\sum_{\mathbf{x}, \mathbf{y}, \mathbf{z}} \delta_{\nu\rho} [\mathcal{G}(z)]_{\Lambda} (C_{\nu\rho}^{K2}(x, y, z) - C_{\nu\rho}^{K1}(x, y, z))}{\sum_{\mathbf{x}, \mathbf{y}} C^{2pt}(x, y)}, \quad (6.20)$$

$$f_{\mathcal{Q}}^{\Delta M_K^{em}} = \text{Tr} \left\{ \lambda_3 \mathcal{Q}^{(em)2} \right\} = \frac{1}{3}.$$

In practice, the integral over z_0 is restricted over the interval $[-t_c, t_c]$, since the contributions for the parts with larger times than the cutoff time t_c are calculated using the elastic part in infinite volume (Eq. (6.15)), as mentioned at the beginning of the section. Additionally, ΔM_K^{em} is calculated for multiple values of t_s , and an exponential fit to the resulting data is used to reconstruct the value for infinite separation times.

Another challenge that arises as part of this calculation is caused by the four-point function of K2 corresponding to the diagram in Fig. 11b. When the two vector currents of this contribution are on top of each other, i.e. if $z_0 = 0$, a large value of the integrand is generated. It can be shown that this corresponds to a logarithmic divergence in the z_0 -integrand of Eq. (6.20) caused by short-distance artifacts that are absent in the continuum. The value of the integral is still finite, but the continuum limit becomes more challenging. As a countermeasure, we have used the neighboring points of the integrand to extrapolate to $z_0 = 0$ via a linear fit. This method reduces the lattice artifacts of the observable considerably and improves the continuum limit.

6.1.4 Lattice results for ΔM_K^{em}

In the following, a value of 1 fm is chosen for the cutoff time t_c , since this choice ensures that (a) the regime where only the elastic term contributes has been reached, (b) finite-size effects are expected to be small and (c) the currents are far enough from the temporal boundaries of the lattice so as not to be affected by them. All of the results presented here are indeed stable under small variations of t_c .

The three points raised above can be addressed using the first plot of Fig. 12. It shows the integrand of Eq. (6.20) for H101 at the largest separation time for large y_t values as well as the elastic part, calculated with the formulas derived in section 6.1.2 for both the finite and infinite volume versions. The finite volume version is in good agreement with the data from the lattice.

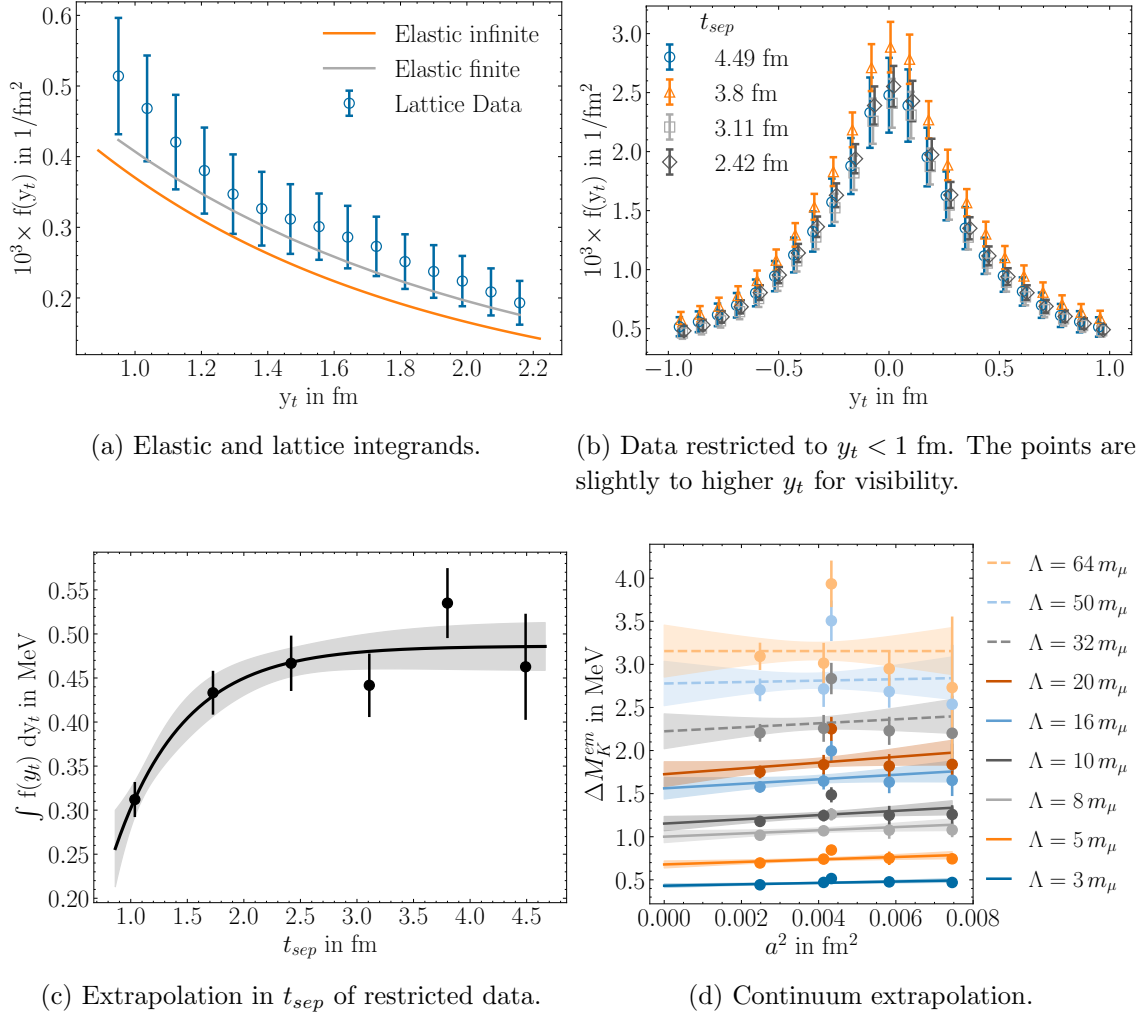


Figure 12: (a) Comparison between the elastic part in finite and infinite volume derived in sec. 6.1.2 and the integrand of Eq. (6.20) calculated on the H101 ensemble for the largest separation time at a PV-mass of $5 m_\mu$. (b) The same integrand of H101 for different separation times with a t_c value of 1 fm. (c) Extrapolation to infinite separation time of the integral over the integrands in (b). (d) Continuum extrapolation of the ΔM_K^{em} values for the different PV-masses. The points from H200 are shown with a slight offset to higher a^2 to make them distinguishable from the points of N202. The resulting values are reported in Table 6.

We have computed $f(x_0)$ for nine values of Λ (see Table 6), since the incremental cost of including an additional value is small. In particular, beyond the ones that were used in computing $a_{\mu,em}^{\text{HVP},38}(\Lambda)$, we have included values as large as $64 m_\mu \simeq 6.8 \text{ GeV}$ in order to study the large- Λ behavior. Note that our final result for $a_{\mu}^{\text{HVP},38}$ only relies on Λ values up to $16 m_\mu$.

Plots (b) and (c) of Fig. 12 show an example of the methodology described previously on the H101 ensemble and with a PV-mass of $\Lambda = 5 m_\mu$. The smallest two separation times

are not shown in Fig. 12b in order to improve visibility. For the second-largest separation time we observe slightly larger results than for the other separation times; we interpret this as an upward statistical fluctuation. In Fig. 12d the continuum limit of the kaon mass splitting value can be seen. For each value of the PV-mass, the ensembles show only very small variations, except for H200. It has significant differences when compared to the other ensembles. This can be explained by its comparatively small volume (see Table 1). Removing it from the extrapolation has no significant impact on the continuum result. For consistency of the data set, we still include this ensemble in the final analysis. The continuum extrapolated values from these fits are reported in Table 6. The integral of the elastic part is already included for these values.

Table 6: Continuum extrapolated values of ΔM_K^{em} . The continuum extrapolation can be seen in Fig. 12d.

Λ/m_μ	ΔM_K^{em} [MeV]	Λ/m_μ	ΔM_K^{em} [MeV]	Λ/m_μ	ΔM_K^{em} [MeV]
3	0.432(21)	10	1.153(83)	32	2.224(202)
5	0.678(41)	16	1.562(124)	50	2.778(257)
8	1.001(69)	20	1.726(144)	64	3.154(302)

The following section will discuss the behavior of the results for the kaon mass splitting in dependence of the PV-mass Λ .

6.1.5 Large Pauli-Villars mass behavior of $\Delta M_K^{em}(\Lambda)$

Starting from Eq. (6.5) the divergent terms for the hadron mass splitting can be obtained by doing an Operator Product Expansion (OPE); see for instance section 4 of Ref. [22]. This yields:

$$\delta M_h(\Lambda) \stackrel{\Lambda \rightarrow \infty}{\underset{z_0 \rightarrow \infty}{\approx}} c_m(\Lambda) \sum_f \mathcal{Q}_f^2 m_f \frac{\partial M_h}{\partial m_f} - c_0(\Lambda) \left(M_h - \sum_f m_f \frac{\partial M_h}{\partial m_f} \right), \quad (6.21)$$

with

$$c_m(\Lambda) = \frac{3\alpha}{2\pi} \left(\log \frac{\Lambda}{\mu_{IR}} + O(\log \log \Lambda) \right) \quad (6.22)$$

$$c_0(\Lambda) = \frac{3\alpha}{2\pi} \left(\frac{1}{48\pi^2 b_0} \log \frac{\Lambda}{\mu_{IR}} + O(\log \log \Lambda) \right). \quad (6.23)$$

Calculating the mass splitting explicitly for the kaon results in the cancellation of many of the terms, leading to

$$\Delta M_K^{em}(\Lambda) \stackrel{\Lambda \rightarrow \infty}{\approx} c_m(\Lambda) f_{\mathcal{Q}}^{\Delta M_K^{em}} m_l \frac{\partial M_K}{\partial m_l} = \mathcal{C} \log \frac{\Lambda}{\mu_{IR}}. \quad (6.24)$$

In the last step, all of the constant factors were summarized in the constant \mathcal{C} , which is approximately 0.12 MeV. The continuum limit for $m_l \frac{\partial M_K}{\partial m_l}$ was obtained using calculations from section 6.2. Using Eq. (6.24) the plausibility of the continuum extrapolated ΔM_K^{em} values in Table 6 can be tested.

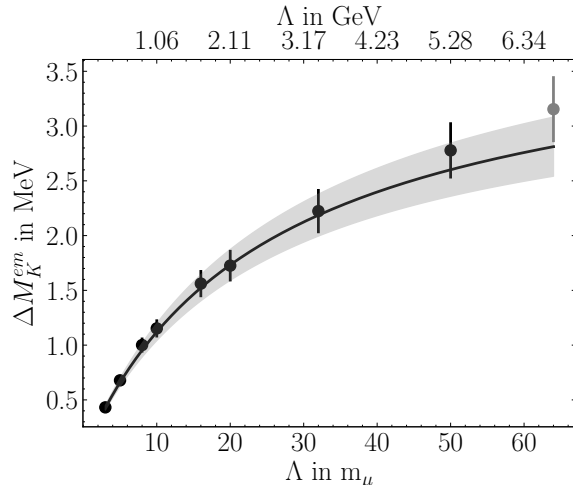


Figure 13: Plot of the continuum extrapolated values of ΔM_K^{em} in dependence of the Pauli-Villars mass. A fit to the data, where the fit function is given by Eq. (6.25), with its corresponding error bands is also shown. This fit function respects the expected behavior of ΔM_K^{em} as obtained by an Operator Product Expansion. The point with the largest PV-mass is marked as gray as it shows cutoff effects and is excluded from the fit.

Fig. 13 shows the values from Table 6 together with a fit. The fit function inspired by Eq. (6.24) is given by

$$f_{fit}(\Lambda) = c_0 \frac{\Lambda}{\Lambda + c_1} + \mathcal{C} \log\left(\frac{\Lambda + c_2}{c_2}\right). \quad (6.25)$$

The point with the largest PV-mass, $\Lambda = 64 m_\mu$, was excluded from the fit, as we suspect it could be affected by cutoff effects. It is marked in gray in Fig. 13. Since the different values for ΔM_K^{em} are obtained by using a different parameter for Λ in the calculation of the photon propagator, the results given in Table 6 are highly correlated. Because of this we use a correlation of 0.9 between all of the input parameters for the fit. This value comes from calculating the correlation of the separation-time extrapolated results on each ensemble; for all of them this correlation was consistently around 0.9. The resulting χ^2/DOF of the fit is 0.92. The factor in front of the logarithmic term in the fit function is set to the value which was predicted via the OPE. In addition to the logarithmic term, a second term, which is linear for small values of Λ and constant for large values, has to be added. This fit function vanishes for $\Lambda = 0$, which has to be the case since the photon propagator is zero in that limit.

We note that one can also reproduce the mass splittings with simpler fits. If only the first term of Eq. (6.25) is used, the resulting fit has a χ^2/DOF of 0.84. Alternatively, it is also possible to use only the second term as a fit function. In that case \mathcal{C} is determined by the fit, instead of setting it to 0.12 MeV. This ansatz results in a χ^2/DOF of 0.96. But the extracted value of \mathcal{C} is 1.29(19) MeV, which is about one order of magnitude higher than the value predicted by the OPE.

The latter fit ansatz assumes that the dominant Λ -dependence of ΔM_K^{em} is given by the divergent term of the inelastic part. But appendix D.3 shows that the elastic part ΔM_K^{elast} still has a sizable dependence on the PV-mass. ΔM_K^{elast} is defined as the part resulting from the elastic contribution to the forward Compton amplitude on the kaon. It goes from a value of 1.53 MeV for $\Lambda = 16 m_\mu$ to 2.4 MeV for infinite Λ . Comparing this to the continuum extrapolated value of ΔM_K^{em} in Table 6, which is 1.562(124) MeV for $\Lambda = 16 m_\mu$, it becomes clear that our lattice results in this section are not precise enough to resolve the Λ -dependence of the divergent term underneath the corresponding dependence of the elastic contribution.

6.2 The response of the kaon mass to an up/down quark mass splitting

The electromagnetic kaon mass splitting from the previous section is part of the effort to fix the bare mass splitting of the light quarks in order to calculate the counterterm. The second part of this calculation is the mass insertion into the charged kaon propagator. For the ensembles with open boundary conditions, this calculation is relatively straightforward. Again, the two-point function from Eq. (6.17) is needed. Additionally, a three-point function has to be calculated,

$$C_{3pt}(x, y, z) = -\text{Re}\langle \text{Tr}[S^l(y, z)\mathbb{1}S^l(z, x)\gamma_5 S^s(x, y)\gamma_5] \rangle_U. \quad (6.26)$$

The source and sink of the kaon are set to specific time slices and projected to zero momentum, with a setup similar to our calculation of the kaon mass splitting: $x_0 = -t_s/2$ and $y_0 = t_s/2$. Ideally the matrix element would be calculated with

$$\langle K^+ | \bar{u}u - \bar{d}d | K^+ \rangle = \lim_{t_s \rightarrow \infty} \frac{a^3 \sum_{\mathbf{y}, \mathbf{z}} C_{3pt}(x, y, z)}{\sum_{\mathbf{y}} C_{2pt}(x, y)} \Big|_{z_0=0}. \quad (6.27)$$

In practice there are two methods. For the first one, the expression of Eq. (6.27) is implemented as closely as possible by calculating the n -point functions for as large separation times as possible. Following this, the sum over the spatial components of z is carried out and a constant fit to the central plateau in the coordinate z_0 is performed: the z_0 values entering the fit are chosen between the source and sink, sufficiently far away from $-t_s/2$ and $t_s/2$.

The second method instead uses a different approach. First the sum over the lattice data for different separation times is computed:

$$S(t_s) = a^4 \sum_{z_0=-t_s/2+a}^{t_s/2-a} \frac{\sum_{\mathbf{y}, \mathbf{z}} C_{3pt}(x, y, z)}{\sum_{\mathbf{y}} C_{2pt}(x, y)}. \quad (6.28)$$

It is important to note that the sum goes over all z_0 values between the source and sink. This sum follows the relation [41]

$$S(t_s) = b + t_s \langle K^+ | \bar{u}u - \bar{d}d | K^+ \rangle + \mathcal{O}(e^{-\Delta t_s}) \quad (6.29)$$

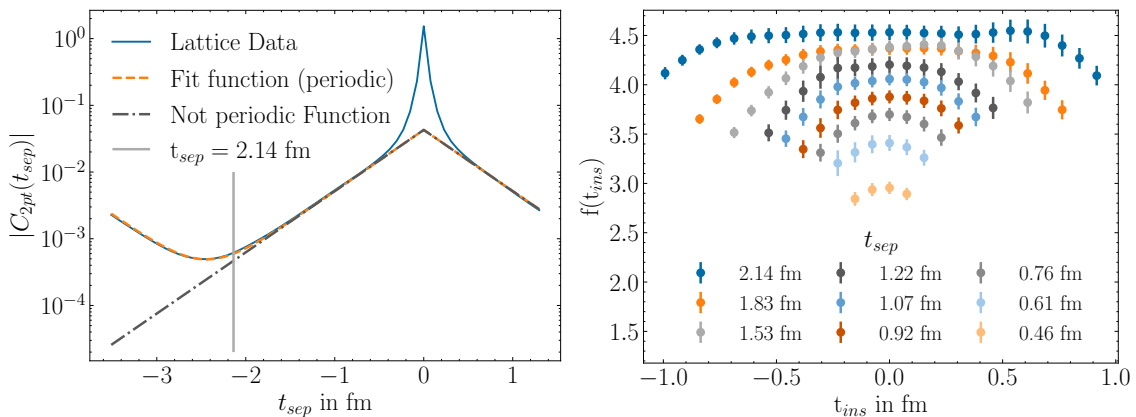
with Δ the relevant mass gap, which means the matrix element can be obtained via a linear fit to the calculated values of $S(t_s)$. In the steps following this section, we use the values

obtained from fitting the plateau to a constant, while the results of the summation method will serve as a cross-check for these values.

For lattices with periodic boundary conditions, which in the present calculations only affects the ensemble B450, an additional treatment of the two-point function becomes necessary due to wrap-around effects. In particular, at t_s equal to half the time extent of the lattice, these effects result in an additional factor of two. To correct for this, an exponential fit that takes into account the periodicity is performed to the lattice data sufficiently far away from the source position of the kaon. The ratio between this exponential fit function and the equivalent function in infinite volume, where no wrap-around effects are present, can be expressed via

$$\frac{C_{2pt}^{fit}(x, y)}{C_{2pt}^{fit, \infty}(x, y)} \underset{t_s \rightarrow \infty}{\approx} 1 + e^{-M(T-2t_s)}. \quad (6.30)$$

The parameter M is taken from the aforementioned fit and T is the time extent of the ensemble, which for B450 is $64a$. The ratio is used to correct the normalizing factor for the matrix element in Eq. (6.27). With the additional steps, B450 reaches the same precision as the other ensembles which can be seen in Table 7.



(a) Calculation of the non periodic two-point function for B450. (b) Lattice data for different separation times for B450.

Figure 14: The data of B450 used for the fits seen in Fig. 15. The step on the left side is only necessary for B450 since the other ensembles have open boundary conditions in time.

6.2.1 Lattice results for $\partial\Delta M_K/\partial(m_u - m_d)$ and comparison with chiral perturbation theory

Fig. 14a shows the previously described way of calculating the two-point function for the lattices with periodic boundary conditions. The difference between the periodic fit and the non periodic function is clearly visible at separation times, which are relevant for our calculation. On the right-hand side, Fig. 14b shows the result for the ratio between the two- and three-point function for different values of t_s for the ensemble B450. One can observe the trend that the data series approaches a plateau for larger and larger separation

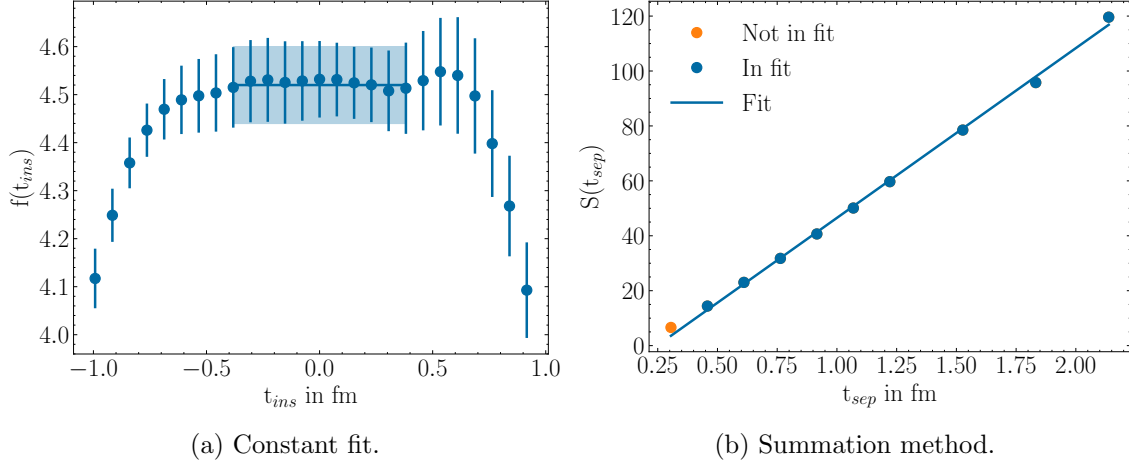


Figure 15: Fits performed to extract the kaon isovector scalar matrix element from the lattice data of B450. (a) Constant fit for the largest calculated source-sink separation t_s , together with the error bands of the fit; see Eq. (6.27). (b) Fit of the summation method, Eq. (6.29), the kaon matrix element corresponding to the slope. The resulting values for both methodologies and all ensembles are collected in Table 7.

times. The fits for the two ways of extracting the matrix element can be seen in Fig. 15. The values obtained for all ensemble are provided in Table 7. There is very good agreement between the results obtained by the constant fit method and the summation method for all ensembles except B450. It has a bit less than 2σ discrepancy between the two values. Because of the periodic boundary conditions of B450, the maximal separation times are much more limited compared to the other ensembles. This is a challenge for both methods. Based on the following two observations we continue using the result of the constant fit method for B450 without further modifications. Firstly, if one performs an extrapolation to infinite separation time with the data in Fig. 14b one recovers up to rounding errors the result of the constant fit at the largest separation time. Secondly, the change in the results quoted in Table 9 is one order of magnitude smaller than the errors, if one just changes to the summation method for B450. If the method is changed for all ensembles the results change even less.

One can use a leading-order chiral perturbation theory (ChPT) prediction in order to check the plausibility of the values calculated in this section. If m_l is the average up/down

Table 7: Values of the light-quark mass derivative of the kaon mass for the different ensembles.

$\partial\Delta M_K/\partial(m_u - m_d)$	N300	N202	H200	B450	H101
Constant fit	4.90(6)	4.67(4)	4.69(7)	4.52(8)	4.11(5)
Summation Method	4.82(5)	4.65(4)	4.77(11)	4.72(7)	4.10(5)

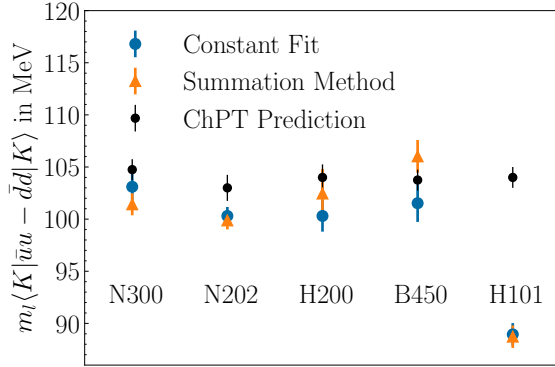


Figure 16: Comparison between the ChPT prediction from Eq. (6.31) and the calculated values of the matrix element for each ensemble.

quark mass, the prediction can be expressed as

$$m_l \frac{\partial \Delta M_K}{\partial(m_u - m_d)} \approx \frac{M_\pi^2}{4M_K}. \quad (6.31)$$

This particular quantity can also be obtained from our lattice results. Until now, we have only used the bare (subtracted) versions of the light-quark masses m_l and the operator $(\bar{u}u - \bar{d}d)$. But for this consistency check we need their improved and renormalized versions. From [42] we get the following relation for the product of these two at the $SU(3)_f$ -symmetric point:

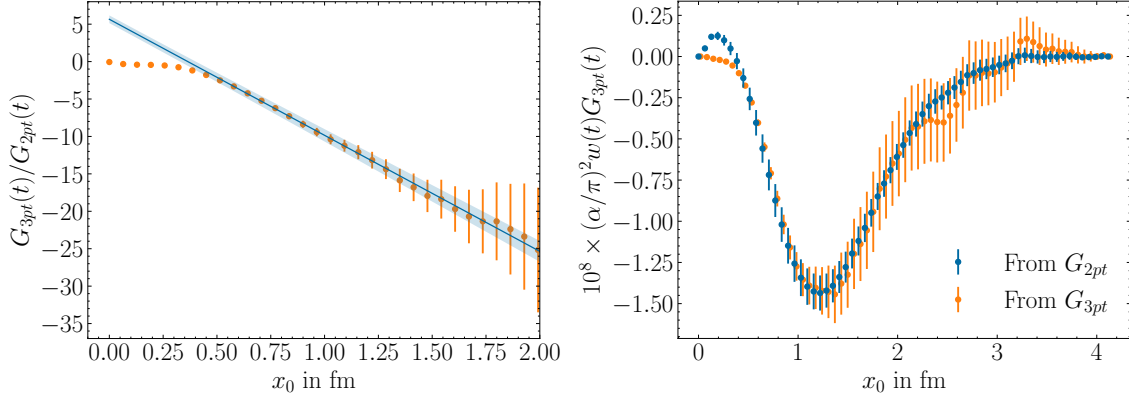
$$[m_l(\bar{u}u - \bar{d}d)]_{I,R} = r_m m_l(\bar{u}u - \bar{d}d)[1 + \mathcal{O}(am_l)]. \quad (6.32)$$

We will not consider the $\mathcal{O}(am_l)$ effects, which means we only need to multiply our results with r_m . The necessary values of r_m can be extracted from [43]. The comparison between the calculated values and the ChPT prediction are shown in Fig. 16. The predictions and their respective uncertainties are calculated from the masses found in Table 1. All ensembles except for H101 show agreement between the calculated values and the prediction. H101 is the ensembles with the largest lattice spacing, which means with the largest $\mathcal{O}(am_l)$ effects. From this we can conclude that our results of this part of the counterterm are plausible.

6.3 The light-quark mass derivative of the HVP

The last missing ingredient to obtain the counterterm is the light-quark mass derivative of the HVP. In comparison to the CCS method from sections 4 and 5, here, the time momentum representation (TMR) of the HVP is used [28]. Additionally, for the data in this section stochastic wall sources were used in order to increase statistics [35]. The master formula for this observable is

$$\frac{\partial a_\mu^{\text{HVP},38}}{\partial(m_u - m_d)} = \frac{1}{2} \frac{\partial a_\mu^{\text{HVP}}}{\partial(m_u - m_d)} = \left(\frac{\alpha}{\pi}\right)^2 \int_0^\infty dx_0 w(x_0) G_{3pt}(x_0). \quad (6.33)$$



(a) Linear fit to the ratio of the two- and three-point function. (b) Comparison between the two methods of extracting the three-point function

Figure 17: (a) Example of the linear fit to the ratio of Eqs. (6.36) and (6.37) on N202. (b) Integrand of equation (6.33) for N202. The yellow dots were obtained by calculating the three-point function directly, while the blue dots were calculated from the two-point function, by multiplying it with the linear term from the fit on the left hand side.

The kernel $w(x_0)$ is taken from the appendix of [44] and $G_{3pt}(x_0)$ is given by

$$G_{3pt}(x_0) = -\frac{2}{3} f_{\mathcal{Q}}^{3pt} a^7 \sum_{i=1}^3 \sum_{\mathbf{x}} \sum_z \text{Re} \langle \text{Tr} [S(0, x) \gamma_i S(x, z) \mathbb{1} S(z, 0) \gamma_i] \rangle_U. \quad (6.34)$$

In this case the charge factor $f_{\mathcal{Q}}^{3pt} = (1/2) \text{Tr} \{ \mathcal{Q}^{(3)} \mathcal{Q}^{(em)2} \} = 1/12$. This three-point function has large uncertainties for large values of x_0 . However, it is possible to derive a relation between the three-point function and the two-point function⁵

$$G_{2pt}(x_0) = \frac{1}{3} f_{\mathcal{Q}}^{2pt} a^3 \sum_{i=1}^3 \sum_{\mathbf{x}} \text{Re} \langle \text{Tr} [S(0, x) \gamma_i S(x, 0) \gamma_i] \rangle_U, \quad (6.35)$$

which can be calculated with higher accuracy ($f_{\mathcal{Q}}^{2pt} = (1/2) \text{Tr} \{ \mathcal{Q}^{(em)2} \} = 1/3$). For large x_0 , and in our range of box sizes $L \lesssim 4$ fm, the two-point function is approximated by

$$G_{2pt}(x_0) \stackrel{x_0 \rightarrow \infty}{\approx} A e^{-Mx_0}. \quad (6.36)$$

Keeping in mind that both A and M depend on the light-quark mass difference, Eq. (6.36) can be used to derive a similar approximation for the three-point function

$$G_{3pt}(x_0) = \frac{\partial G_{2pt}(x_0)}{\partial(m_u - m_d)} \stackrel{x_0 \rightarrow \infty}{\approx} (A' - B'x_0) e^{-Mx_0}. \quad (6.37)$$

Here, it is important to note that the exponents of the approximations are the same. So the values of the three-point function can be obtained from the two-point function by

⁵At the $SU(3)_f$ symmetric point, the expression $2 \left(\frac{\alpha}{\pi}\right)^2 \int_0^\infty dx_0 w(x_0) G_{2pt}(x_0)$ yields the isoQCD contribution of the up, down and strange quarks to a_μ^{HVP} .

Table 8: Values of the light-quark mass difference derivative of the HVP for the different ensembles, as well as the ratio R_{38K} obtained using the kaon matrix element values from the constant fit.

	N300	N202	H200	B450	H101
$10^{11} \times \frac{\partial a_{\mu}^{\text{HVP},38}}{\partial(m_u-m_d)}$ [1/MeV]	-7.37(79)	-9.32(85)	-7.05(93)	-6.89(37)	-7.58(64)
$10^{11} \times R_{38K}$ [1/MeV]	-1.50(17)	-1.99(19)	-1.50(20)	-1.52(9)	-1.84(16)

multiplying it with a first-order polynomial in x_0 . The coefficients of this term can be obtained from a linear fit to the ratio of the three- and two-point functions.

This ratio together with a fit is shown in Fig. 17a for the N202 ensemble. The upper limit of the fit range was set to 2 fm. Multiple models using different lower limits were considered. The weights by which they contribute were determined using the Akaike Information Criterion [45, 46]. The right-hand side of the same figure, Fig. 17b, depicts the integrand of Eq. (6.33) on the same ensemble, both from the three-point function directly and from the two-point function using the fit from the left hand side. For very small values of x_0 , where higher mass states are still important, there is a sizable discrepancy between the two methods. But already at 0.5 fm both methods have equal values within the error. At first the uncertainties of the values from the three-point function are smaller, but around 1 fm this switches and stays this way until the upper limit. The other ensembles have the same behavior.

Based on these observations we will use a hybrid method for the results presented in this section and for the subsequent calculations. For the integrand below 1 fm, the three-point function from Eq. (6.34) is used directly. For x_0 values larger than that, we use the approximation from the two-point function of Eq. (6.35). The results are collected in Table 8.

Similar to section 6.2 the periodic boundary conditions in the time direction of B450 need to be accounted for. In comparison to the other ensembles the integral is not saturated when the maximal time extend is reached. We use the same methodology as before, where a fit respecting the periodicity is performed to the two-point function. This is then used to calculate the corresponding non-periodic version of the two-point function, which is fed into the integral. Here, the correction is small compared to the error, the value of the integral goes from $-6.74(36)$ 1/MeV to $-6.89(37)$ 1/MeV, but this change is still noticeable during the continuum extrapolation of R_{38K} , slightly reducing the χ^2 .

6.3.1 The ratio R_{38K} , and the strong IB contribution in the FLAG24 scheme

An important physical quantity is the ratio R_{38K} introduced in Eq. (2.14). We recall that it expresses the response of the vacuum polarization contribution to a kaon mass splitting, at fixed isospin-averaged pion, kaon and scale setting quantity (typically a baryon mass). The results from this section and section 6.2 can be used in order to calculate this ratio for each gauge ensemble. It is the ratio between the light-quark mass derivative of the

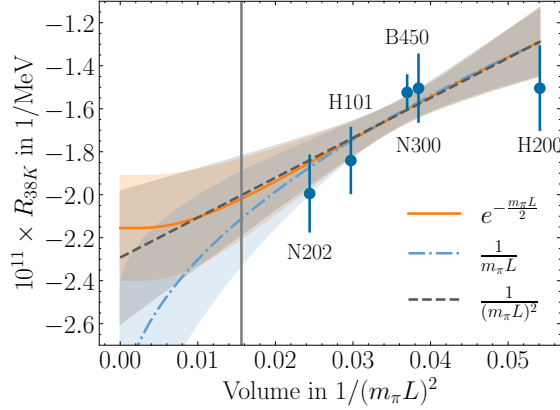


Figure 18: Extrapolation of R_{38K} to infinite volume. The vertical line is located at the reference volume of $m_\pi L = 8$. Three different fits using the general ansatz of Eq. (6.38) are shown. The labels give the volume term for each fit respectively. The χ^2/DOF of the fits together with their values at the reference volume are written in Table 9.

HVP and the light-quark mass derivative of the kaon mass (see Eq. (2.14) and (A.5)). The resulting values are given in Table 8.

At fixed physical volume, we do not observe any statistically significant dependence on the lattice spacing (compare in particular the results on ensembles B450 and N300), while the volume dependence is clearly significant: see Fig. 18. We therefore employ a fit ansatz for extrapolating to infinite volume of the form

$$f_{fit}(m_\pi L) = c_0 + c_1 f_{vol}(m_\pi L) . \quad (6.38)$$

Asymptotically at large L , one would expect the volume term to be given by $f_{vol}(m_\pi L) = e^{-m_\pi L}$, but this expression does not describe our data well. Instead we use three different ansätze given in the first column of Table 9. All of them have χ^2/DOF close to one. We will use them to extrapolate R_{38K} to a reference volume of $m_\pi L = 8$. The last part of the extrapolation to infinite volume is then given as a correction calculated in scalar QED. For the value at the reference volume, we take the mean of the extrapolations, which gives us

$$R_{38K}(m_\pi L = 8) = -2.04(22)_{\text{stat}}(10)_{\text{syst}} \times 10^{-11} \text{ MeV}^{-1} . \quad (6.39)$$

The correction to get to infinite volume vanishes completely within the error and has a value of $-0.006(60) \text{ MeV}^{-1} \times 10^{-11}$. The error was chosen in order to have a very conservative estimate. With this, the continuum extrapolated result of R_{38K} is given by

$$R_{38K} = -2.05(22)_{\text{stat}}(12)_{\text{syst}} \times 10^{-11} \text{ MeV}^{-1} . \quad (6.40)$$

In the FLAG24 report [47], specific values for the reference hadron masses ($M_{\pi^+}, M_{K^+}, M_{K^0}$) are given in a QCD world with $m_u \neq m_d$, electromagnetism being ‘switched off’. These choices correspond to a scheme for separating electromagnetic from strong isospin-breaking effects. Since $\Delta M_K = -6 \text{ MeV}$ per definition in that ‘world’, the strong IB contribution

Table 9: χ^2/DOF and value at the reference volume of the different fit ansätze in Fig 18. The general form of the fit functions can be found in Eq. (6.38).

f_{vol} Ansatz	χ^2/DOF	$10^{11} \times R_{38K}(m_\pi L = 8)$ [1/MeV]
$e^{-\frac{m_\pi L}{2}}$	1.08	-2.02(19)
$\frac{1}{m_\pi L}$	0.95	-2.11(22)
$\frac{1}{(m_\pi L)^2}$	1.16	-2.00(19)

to $a_\mu^{\text{HVP},38}$ is given by

$$a_{\mu,SIB}^{\text{HVP},38} = -6 \text{ MeV} \times R_{38K} = 12.30(1.32)_{\text{stat}}(72)_{\text{syst}} \times 10^{-11}. \quad (6.41)$$

6.4 The quantity $a_\mu^{\text{HVP},38}(\Lambda)$, continuum extrapolated at fixed Λ

We can now combine the results of the previous sections in order to calculate the total contribution $a_\mu^{\text{HVP},38}$ based on Eqs. (2.10–2.12). For that we use the continuum extrapolated values of $a_\mu^{\text{HVP},38}(\Lambda)$, $\Delta M_K^{em}(\Lambda)$ and R_{38K} , which are summarized in Table 10. It is important to note that $a_{\mu,(2+2)a}^{\text{HVP},38}$ and R_{38K} in rows three and five are independent of the PV-mass. The last two rows show the counterterm and the total contribution $a_\mu^{\text{HVP},38}$ in dependence of Λ , respectively. From this one can observe that the result and its error are completely dominated by the counterterm. The bare electromagnetic contributions $a_{\mu,(4)}^{\text{HVP},38}$ and $a_{\mu,(2+2)a}^{\text{HVP},38}$ are only small corrections which vanish within the error. Still, the data provides a hint that the connected part $a_{\mu,(4)}^{\text{HVP},38}$ cancels out the logarithmic divergence of the counterterm, bringing the total result of the smallest PV-mass and of the largest PV-mass closer together. Fig. 19 shows a plot of the residual dependence on Λ of the total contribution $a_\mu^{\text{HVP},38}$. The extrapolation to infinite PV-mass is very flat, all of the points being equal to one another within the errors.

We remark that in continuum field theory, typically the approach to the $\Lambda = \infty$ limit occurs with leading $O(1/\Lambda^2)$ corrections. In the future, it could be interesting to evaluate the elastic contribution to the kaon mass splitting directly at $\Lambda = \infty$, maintaining the

Table 10: Continuum extrapolated values of the different contributions to $a_\mu^{\text{HVP},38}$. All values except ΔM_K^{em} are multiplied by 10^{11} .

PV-mass	$\Lambda = 3 m_\mu$	$\Lambda = 5 m_\mu$	$\Lambda = 10 m_\mu$	$\Lambda = 16 m_\mu$
$a_{\mu,(4)}^{\text{HVP},38}(\Lambda)$	-0.006(39) _{st.}	0.002(74) _{st.}	-0.068(193) _{st.}	-0.249(321) _{st.}
$a_{\mu,(2+2)a}^{\text{HVP},38}$	-0.53(17) _{st.}	-0.53(17) _{st.}	-0.53(17) _{st.}	-0.53(17) _{st.}
ΔM_K^{em} [MeV]	0.432(21) _{st.}	0.678(41) _{st.}	1.153(83) _{st.}	1.562(124) _{st.}
R_{38K} [1/MeV]	-2.05(22) _{st.} (12) _{sy.}	-2.05(22) _{st.} (12) _{sy.}	-2.05(22) _{st.} (12) _{sy.}	-2.05(22) _{st.} (12) _{sy.}
$C_T(\Lambda)$	8.95(97) _{st.} (53) _{sy.}	9.45(1.02) _{st.} (56) _{sy.}	10.43(1.14) _{st.} (61) _{sy.}	11.27(1.24) _{st.} (66) _{sy.}
$a_\mu^{\text{HVP},38}(\Lambda)$	8.41(98) _{st.} (53) _{sy.}	8.93(1.04) _{st.} (56) _{sy.}	9.83(1.16) _{st.} (61) _{sy.}	10.49(1.29) _{st.} (66) _{sy.}

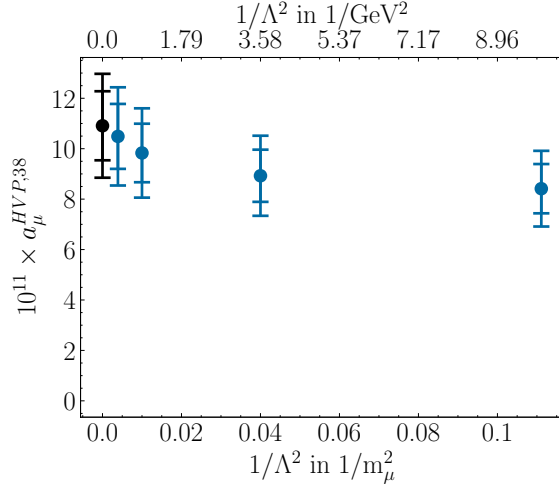


Figure 19: PV-mass extrapolation of $a_\mu^{\text{HVP},38}$. The inner horizontal bars show the statistical error, while the outer bar shows the additional systematic error. The black dot shows the result of a extrapolation linear in $1/\Lambda^2$ using the two points with the largest PV-masses. A correlation coefficient of one was assumed between them.

regulator only for the inelastic part, the idea being to reduce any residual Λ dependence in $a_\mu^{\text{HVP},38}(\Lambda)$ even further.

6.5 Comparison of lattice results and model estimates

Appendix D provides estimates from a hadronic model for the various quantities computed on the lattice. For convenience we have collected them in Table 11, where for the Λ -dependent quantities we have set $\Lambda = 16 m_\mu$ in the first line. In the second line the PV-mass is infinite. The main observations are that the bare electromagnetic correction is very small, below 1×10^{-11} , and the model estimate for $a_\mu^{\text{HVP},38}$ is consistent with the lattice result. The most important quantity, R_{38K} , is somewhat underestimated in magnitude by the model, but nevertheless consistent within the uncertainties. The elastic part, of size 1.53 MeV when evaluated at $\Lambda = 16 m_\mu$, appears to saturate the electromagnetic kaon mass splitting computed on the lattice with the same value of Λ .

Table 11: Hadronic-model estimate for a PV-mass of $\Lambda = 16 m_\mu$ in the first line, and for infinite PV-mass in the second line. All values except $\Delta M_K^{\text{elast}}$ are multiplied by 10^{11} .

$a_{\mu,em}^{\text{HVP},38,\text{low}}$	$\Delta M_K^{\text{elast}}$ [MeV]	R_{38K} [1/MeV]	$a_\mu^{\text{HVP},38}$
-0.25(0.4)	1.53	-1.53(38)	8.1(2.1) $_{R_{38K}}$ (0.4) $_{\text{em}}$ (0.4) $_{\text{sd}}$
0.01(0.6)	2.4	-1.53(38)	9.7(2.4) $_{R_{38K}}$ (0.6) $_{\text{em}}$ (0.6) $_{\text{sd}}$

7 Conclusion

In this paper, we have performed a lattice QCD calculation of the isospin-violating part of the hadronic vacuum polarization (HVP), which corresponds to the cross-terms in the two-point correlation function of the electromagnetic current j_μ^{em} , when the latter is written as the sum of an isovector (j_μ^3) and an isoscalar (j_μ^8) current. It would vanish for equal up and down quark masses in the absence of electromagnetic effects. Our result for the isospin-violating HVP contribution to the anomalous magnetic moment of the muon, at the $SU(3)_f$ symmetric point, reads:

$$2 a_\mu^{\text{HVP},38} = 21.8(2.8)_{\text{stat}}(1.4)_{\text{syst}} \times 10^{-11} \quad (M_\pi = M_K \simeq 416 \text{ MeV}), \quad (7.1)$$

where the factor of two on the left-hand side accounts for the equally sized (3,8) and (8,3) contributions.

In order to deal with the long-range electromagnetic effects on the lattice, we have used a Pauli-Villars (PV) regulated photon propagator with the cutoff scale Λ set above the typical hadronic scale of 1 GeV. Our results, however, exhibit little dependence on the cutoff, compared to the uncertainties. We account for the residual dependence on the PV-mass by performing a linear fit in $1/\Lambda^2$ on the results of the two largest PV-masses to get our result for $\Lambda \rightarrow \infty$.

The PV regularization enables us to do crosschecks of our intermediate results. For the connected diagrams, we were able to obtain consistent results between lattice calculations on ‘gluonless’ ensembles and continuum QED calculations. For the charged/neutral kaon mass splitting, which was part of the (mass) counterterm, our results are consistent with the expected logarithmic dependence on Λ . This expectation resulted from an Operator Product Expansion. In addition, we were able to compare the bare electromagnetic correction $a_{\mu,em}^{\text{HVP},38}(\Lambda)$ to continuum model predictions based on the kaon loop and pseudoscalar meson exchanges.

In general, an advantage of decoupling the photon cutoff Λ from the lattice QCD cutoff $1/a$ is that intermediate results such as $a_{\mu,em}^{\text{HVP},38}(\Lambda)$ and $\Delta M_K^{em}(\Lambda)$ no longer depend on the lattice action employed and can be reused, or cross-checked, by other lattice collaborations. By contrast, when Λ is identified with $1/a$ by using a lattice photon propagator, as has been the case in most previous lattice calculations of QED effects, the quantities $a_{\mu,em}^{\text{HVP},38}(1/a)$ and $\Delta M_K^{em}(1/a)$ depend on the details of the lattice QCD action used.

We have also pointed out the importance of precisely determining the quantity R_{38K} defined in Eq. (2.14), a scheme-independent and renormalization group invariant quantity. Based on the results presented here, an extension of our lattice calculations towards physical pion and kaon masses seems promising. In this case, the additional disconnected diagrams will become relevant – see Fig. 3. Still, we expect the elastic contribution to the counterterm to remain the numerically dominant part.

We have complemented our lattice calculations by hadronic-model estimates of R_{38K} and of the low-energy part $a_{\mu,em}^{\text{HVP},38,\text{low}}$ of the vacuum polarization – see section 6.5, and Appendix D for details. We have found agreement within the uncertainty of 25% of the model with our lattice QCD results. This emboldens us to attempt an estimate at physical

pion and kaon masses. Our estimate of R_{38K} is consistent with previous phenomenological results [48, 49], and we arrive at an estimate of

$$2 a_\mu^{\text{HVP},38} = 32(8) \times 10^{-11} \quad ((M_\pi, M_K) \text{ physical; hadronic model}) \quad (7.2)$$

for the total isospin-violating part of the hadronic vacuum polarization in the muon ($g-2$). Clearly it is a relevant effect worth bringing under control, given the current precision (22×10^{-11}) of the world average for the direct measurement of a_μ [1–3].

Acknowledgments

We thank Simon Kuberski for providing the data for the calculation of the HVP light-quark mass derivative. We also thank Franziska Hagelstein for an ongoing collaboration on computing electromagnetic corrections to hadronic vacuum polarization. We acknowledge the support of Deutsche Forschungsgemeinschaft (DFG) through the research unit FOR 5327 “Photon-photon interactions in the Standard Model and beyond exploiting the discovery potential from MESA to the LHC” (grant 458854507), and through the Cluster of Excellence “Precision Physics, Fundamental Interactions and Structure of Matter” (PRISMA+ EXC 2118/1) funded within the German Excellence Strategy (project ID 39083149). Calculations for this project were partly performed on the HPC cluster and “HIMster II” at the Helmholtz-Institut Mainz and “Mogon II” at JGU Mainz. We are grateful to our colleagues in the CLS initiative for sharing ensembles.

A Derivation of the expression for the counterterm to $a_\mu^{\text{HVP},38}$

The expression for the kaon mass splitting $\Delta M_K \equiv M_{K^+} - M_{K^0}$, expanded to leading order in α and $(m_u - m_d)$ around an isosymmetric point in the parameter space of QCD, reads

$$\Delta M_K^{\text{phys}} = \Delta M_K^{\text{em}}(\Lambda) + (m_u - m_d)(\Lambda) \frac{\partial \Delta M_K}{\partial (m_u - m_d)}. \quad (\text{A.1})$$

The partial derivative is taken at fixed $(m_u + m_d)$ and m_s , as well as at fixed bare (QCD) coupling g_0 and at $\alpha = 0$: the right-hand side is an expansion in the bare parameters of QCD+QED. Since the splitting is isospin breaking, only one counterterm, associated with the quark-mass difference $(m_u - m_d)$, appears. We thus interpret Eq. (A.1) as a natural renormalization condition that determines the bare parameter $(m_u - m_d)(\Lambda)$.

In the past, the cutoff Λ on the photon propagator has been identified with the lattice cutoff $1/a$ by computing this propagator on the lattice. In our approach, the scale Λ , which appears in the Pauli-Villars regularization terms of the photon propagator (see Eq. (2.9)), is decoupled from the lattice spacing. Thus, at fixed Λ each term in Eq. (A.1) has a continuum limit.

The analogous expansion for $a_\mu^{\text{HVP},38}$ is

$$a_\mu^{\text{HVP},38} = a_{\mu,\text{em}}^{\text{HVP},38}(\Lambda) + (m_u - m_d)(\Lambda) \frac{\partial a_\mu^{\text{HVP},38}}{\partial (m_u - m_d)}. \quad (\text{A.2})$$

Eliminating the bare parameter $(m_u - m_d)(\Lambda)$ using Eq. (A.1), we arrive at

$$a_\mu^{\text{HVP},38} = a_{\mu,em}^{\text{HVP},38}(\Lambda) + \frac{\Delta M_K^{\text{phys}} - \Delta M_K^{\text{em}}(\Lambda)}{\frac{\partial \Delta M_K}{\partial (m_u - m_d)}} \frac{\partial a_\mu^{\text{HVP},38}}{\partial (m_u - m_d)}. \quad (\text{A.3})$$

Finally, realizing that the Hamiltonian of QCD can be written

$$H = \int d^3x \left(\frac{1}{2}(m_u - m_d)(\bar{u}u - \bar{d}d) + \text{isosymmetric terms} \right), \quad (\text{A.4})$$

we can trade the partial derivative for a scalar matrix element,

$$\frac{\partial \Delta M_K}{\partial (m_u - m_d)} = \frac{1}{2} (\langle K^+ | \bar{u}u - \bar{d}d | K^+ \rangle - \langle K^0 | \bar{u}u - \bar{d}d | K^0 \rangle) = \langle K^+ | \bar{u}u - \bar{d}d | K^+ \rangle, \quad (\text{A.5})$$

where in the last step we have exploited the isospin symmetry to simplify the expression. The kaon states are at rest ($\mathbf{p} = 0$) and their normalization is the non-covariant one, $\langle K_{\mathbf{p}} | K_{\mathbf{p}'} \rangle = (2\pi)^3 \delta^{(3)}(\mathbf{p} - \mathbf{p}')$. Inserting the simplified expression (A.5) into Eq. (A.3), one arrives at Eq. (2.10) with the counterterm given by Eq. (2.12).

B QED continuum prediction for the connected contribution

A formalism for obtaining the two-loop vacuum polarization in QED via the Cottingham formula has been explained in details in [22]. Here we sketch only the main steps of the vacuum polarization calculation pertinent to a double Pauli-Villars photon regularization and provide its contribution to the muon ($g - 2$).

Using the Cottingham formula, the four-point (two-loop) vacuum polarization can be written in terms of the forward doubly-virtual LbL scattering amplitude $\mathcal{M}(\nu, K^2, Q^2)$ as

$$\Pi_{4\text{pt}}(Q^2, \Lambda) = \frac{1}{3(2\pi)^3 Q^2} \int_0^\infty dK^2 K^2 \left[\frac{1}{K^2} \right]_\Lambda \int_0^1 dx \sqrt{1-x^2} \mathcal{M}(KQx, K^2, Q^2), \quad (\text{B.1})$$

where $K^2 = -k^2$ and $Q^2 = -q^2$ are virtualities of the scattered photons with momenta k and q , correspondingly, and $\nu = k \cdot q = KQx$. Substituting the dispersive representation in the variable ν of the forward LbL amplitude with one subtraction at $\nu = \bar{\nu}$,

$$\mathcal{M}(\nu, K^2, Q^2) = \mathcal{M}(\bar{\nu}, K^2, Q^2) + \frac{2}{\pi} (\nu^2 - \bar{\nu}^2) \int_{\nu_{\text{thr}}}^\infty d\nu' \frac{\nu' \text{Im} \mathcal{M}(\nu', K^2, Q^2)}{(\nu'^2 - \bar{\nu}^2)(\nu'^2 - \nu^2)}, \quad (\text{B.2})$$

and making use of the optical theorem

$$\text{Im} M(\nu, K^2, Q^2) = 2\sqrt{X} \sigma(\nu, K^2, Q^2), \quad (\text{B.3})$$

where $X = \nu^2 - Q^2 K^2$ and $\sigma = 4\sigma_{TT} - 2\sigma_{LT} - 2\sigma_{TL} + \sigma_{LL}$ is an unpolarized $\gamma^* \gamma^*$ -fusion cross section, we arrive at the dispersive representation of the Cottingham formula:

$$\begin{aligned} \Pi_{4\text{pt}}(Q^2, \Lambda) = & \frac{1}{3(2\pi)^3 Q^2} \int_0^\infty dK^2 K^2 \left[\frac{1}{K^2} \right]_\Lambda \left[\frac{\pi}{4} \mathcal{M}(\bar{\nu}, K^2, Q^2) \right. \\ & \left. + \int_{\nu_{\text{thr}}}^\infty d\nu \left(\frac{2}{\nu + \sqrt{X}} - \frac{\nu}{\nu^2 - \bar{\nu}^2} \right) \sqrt{X} \sigma(\nu, K^2, Q^2) \right]. \end{aligned} \quad (\text{B.4})$$

The double Pauli-Villars regularization of the photon propagator (2.9), which is employed on the lattice, corresponds to the following regulator in continuum calculation:

$$\left[\frac{1}{K^2} \right]_{\Lambda} = \frac{\zeta^2 \Lambda^4}{K^2(K^2 + \Lambda^2)(K^2 + \zeta^2 \Lambda^2)}, \quad \zeta = \frac{1}{\sqrt{2}}. \quad (\text{B.5})$$

The contribution to the muon ($g - 2$) that stems from the Cottingham formula reads

$$a_{\mu}^* = -\frac{\alpha_{\text{em}}}{2\pi} \Pi_{4\text{pt}}(0, \Lambda) + \frac{\alpha_{\text{em}}}{\pi} \int_0^{\infty} dQ^2 \mathcal{K}(Q^2) \Pi_{4\text{pt}}(Q^2, \Lambda), \quad (\text{B.6})$$

with the QED kernel \mathcal{K} given by

$$\mathcal{K}(Q^2) = \frac{1}{2m_{\mu}^2} \frac{(v-1)^3}{2v(v+1)}, \quad v = \sqrt{1 + \frac{4m_{\mu}^2}{Q^2}}. \quad (\text{B.7})$$

A numerical evaluation of Eq. (B.6), with the regulator set to $\Lambda = 3 m_{\mu}$ and the mass of the lepton inducing vacuum polarization set to $m_{\ell} = m_{\mu}$, yields

$$a_{\mu}^* \approx 7.499 \times 10^{-11}. \quad (\text{B.8})$$

C Kaon electromagnetic form factor

The kaon electromagnetic form factor enters the calculation of the elastic contribution of the electromagnetic kaon-mass splitting in section 6.1.2. While the form factor is calculable on the lattice directly, we use the vector-meson-dominance (VMD) monopole parametrization (6.16) throughout the paper. In this appendix we argue that the VMD approximation is sufficient for our purposes by comparing the results of the elastic contribution on the H101 ensemble for both methods of obtaining the electromagnetic kaon form factor.

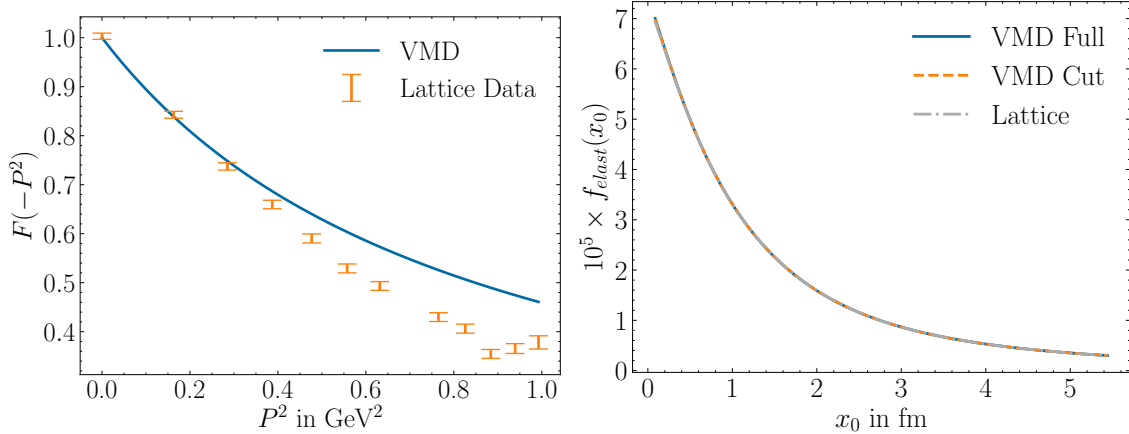
The functional form of the VMD form factor is given by Eq. (6.16).⁶ For the H101 ensemble, following [36], a VMD mass of 921 MeV was used; this value comes from a VMD fit to the π^0 transition form factor on the same ensemble [50].

In order to obtain the form factor from the lattice, we follow the procedure from [41], which is a very similar approach to the summation method in section 6.2, but instead of a unit matrix $\mathbb{1}$ the gamma-matrices γ_j get inserted while calculating the three-point function. Additionally the kaon has to be projected to non-zero momenta. At the $\text{SU}(3)_f$ symmetric point the propagator of the light quarks and the strange quark are the same, which means the two- and three-point functions for this calculation are

$$C_2(\mathbf{p}, x_0) = -a^3 \sum_{\mathbf{x}} e^{-i\mathbf{p}\mathbf{x}} \text{Tr}[S(0, \mathbf{x})\gamma_5 S(\mathbf{x}, 0)\gamma_5], \quad (\text{C.1})$$

$$C_3^{\nu}(\mathbf{p}, x_0, y_0) = -a^6 \sum_{\mathbf{x}, \mathbf{y}} e^{-i\mathbf{p}\mathbf{y}} \text{Tr}[S(0, \mathbf{y})\gamma_{\nu} S(\mathbf{y}, \mathbf{x})\gamma_5 S(\mathbf{x}, 0)\gamma_5]. \quad (\text{C.2})$$

⁶One way to evaluate the expression in finite volume is to use the Gaussian representation $G_m(x) = \frac{1}{16\pi^2} \int_0^{\infty} \frac{dt}{t^2} e^{-tm^2 - x^2/(4t)}$ of the scalar propagator, which allows one to obtain the integrals over the spatial components of x over the interval $[-L/2, L/2]$ in terms of the error function.



(a) VMD vs. lattice form factor.

(b) f_{elast} calculated with different form factors.

Figure 20: Comparison of the kaon form factor as obtained on ensemble H101 to the VMD form factor with $M_{\text{vmd}} = 921$ MeV. On the right hand side, $f_{elast}(x_0)$ is calculated in the finite volume of ensemble H101 using the discrete momentum values $\mathbf{p}^2 = (2\pi/L)^2 \mathbf{n}^2$. For the lattice and the “VMD Cut” curves, the momentum sum is truncated at $\mathbf{p}^2 = 2.4$ GeV², while for “VMD Full” it extends to significantly higher values.

From these the lattice form factor $F_{\text{lat}}(-P^2)$ can be obtained in the following way:

$$\bar{C}_2(\bar{p}, x_0) = \frac{\sum_{\mathbf{p}:|\mathbf{p}|=\bar{p}} C_2(\mathbf{p}, x_0)}{\sum_{\mathbf{p}:|\mathbf{p}|=\bar{p}} 1} \quad (\text{C.3})$$

$$R(\mathbf{p}, x_0, y_0) = \frac{C_3^0(\mathbf{p}, x_0, y_0)}{\bar{C}_2(0, x_0)} \sqrt{\frac{\bar{C}_2(|\mathbf{p}|, x_0 - y_0) \bar{C}_2(0, y_0) \bar{C}_2(0, x_0)}{\bar{C}_2(0, x_0 - y_0) \bar{C}_2(|\mathbf{p}|, y_0) \bar{C}_2(|\mathbf{p}|, x_0)}} \quad (\text{C.4})$$

$$F^{\text{eff}}(\bar{p}, x_0, y_0) = \frac{2\sqrt{M_K E_p}}{M_K + E_p} \frac{\sum_{\mathbf{p}:|\mathbf{p}|=\bar{p}} R(\mathbf{p}, x_0, y_0)}{\sum_{\mathbf{p}:|\mathbf{p}|=\bar{p}} 1} \quad (\text{C.5})$$

$$\Rightarrow a \sum_{y_0=a}^{x_0-a} F^{\text{eff}}(\bar{p}, x_0, y_0) \stackrel{x_0 \rightarrow \infty}{\approx} b(\bar{p}) + x_0 F_{\text{lat}}(-P^2) + \dots \quad (\text{C.6})$$

with $P^2 = 2M_K(\sqrt{\bar{p}^2 + M_K^2} - M_K)$ in our choice of kinematics. Following the last step, a linear fit in x_0 to the resulting data was performed in order to extract the lattice form factor.

We will use the integrand of the elastic contribution in finite volume in order to compare both calculations. The integrand $f_{elast}(x_0)$ is computed based on Eq. (6.14). Note that the maximal value of \mathbf{p}^2 amounts to about 2.4 GeV² in our lattice calculation. For a like-by-like comparison, two versions of the VMD calculation were performed, one for these restricted values of \mathbf{p}^2 and one without this restriction.

The comparison between the VMD form factor and lattice data can be seen in Fig. 20a. For the first three values, the lattice and the VMD form factor are in perfect agreement. From the fourth point onward, the lattice calculation is decreasing more rapidly. However, as one can see on the right-hand-side in Fig. 20b, this discrepancy results in a completely

Table 12: Contributions to $a_{\mu,em}^{\text{HVP},38}(\Lambda = 16 m_\mu)$ at physical quark masses and at the $\text{SU}(3)_f$ symmetric point $M_\pi = M_K \simeq 416 \text{ MeV}$. All contributions in 10^{-11} units.

Contribution:	$a_{\mu,em}^{\text{HVP},38}(\Lambda = 16 m_\mu) _{\text{physpt}}$	$a_{\mu,em}^{\text{HVP},38}(\Lambda = 16 m_\mu) _{\text{SU}(3)_f}$
charged kaon loop (sQED)	-0.16	-0.41
π^0 exchange	0.57	0.21
η exchange	-0.10	-0.21
η' exchange	0.14	0.16
Total	0.45	-0.25

negligible difference for $f_{\text{elast}}(x_0)$ at the Euclidean times of interest. Moreover, there is practically no difference between the limited and full VMD versions.

As the result, we have decided to forgo the systematic lattice calculation of the kaon form factor and use instead the VMD approximation for the calculations in section 6.1.

D Phenomenological estimate of $a_\mu^{\text{HVP},38}$

In this appendix, we derive various predictions for $a_\mu^{\text{HVP},38}(\Lambda)$, $a_{\mu,em}^{\text{HVP},38,\text{low}}$ and R_{38K} based on phenomenological models. We refer the reader to Eqs. (2.10–2.14) and sec. 2.1 for the definition of these quantities. After comparing the predictions to our lattice results at the $\text{SU}(3)_f$ point, we also provide estimates at physical quark masses.

D.1 The bare electromagnetic contribution at fixed photon cutoff Λ

We begin by estimating the bare e.m. contribution $a_\mu^{\text{HVP},38}(\Lambda)$ for a fixed value $\Lambda = 16 m_\mu \simeq 1.69 \text{ GeV}$. We take into account the contributions of the pseudoscalar (PS) meson poles (π^0, η, η'), as well as of the charged kaon loop. We compute the PS-pole contributions using the master formula given in Ref. [22], which involves the meson's transition form factor for spacelike photon virtualities. We use the vector-meson dominance (VMD) parametrization of the form factor, with the parameters chosen as in Ref. [15]. As compared to the full a_μ^{HVP} , we give the pion contribution a factor 1/4 in $a_\mu^{\text{HVP},38}$. For the (η, η') contributions, we proceed as follows⁷: at the $\text{SU}(3)_f$ symmetric point, the flavour symmetry dictates that the η' receive a factor 3/16 and the η a factor (-3/4), which leads to a complete cancellation between the η and the π^0 exchanges. At the physical point, we treat the η and η' as linear superpositions of the octet and singlet states with a mixing angle as in Ref. [15]. As for the kaon loop, we evaluate it in the scalar QED approximation using the expressions given in appendices A and B of Ref. [15], applying to it a factor 1/4 relative to its contribution in a_μ^{HVP} , due to the charge of K^\pm with respect to the currents j_λ^3 and j_λ^8 . The results are collected in Table 12.

⁷For the pion, the factor applied follows from the approximation that the TFF with respect to one isovector and one isoscalar current is approximated by $\mathcal{F}_{\pi^0 38}(q_1^2, q_2^2) \simeq (1/2)\mathcal{F}_{\pi^0 \gamma^* \gamma^*}(q_1^2, q_2^2)$. For the isoscalar PS mesons, we have $\mathcal{F}_{P \gamma^* \gamma^*} = \mathcal{F}_{P33} + \mathcal{F}_{P88}$; at the $\text{SU}(3)_f$ point, this implies $\mathcal{F}_{P88} = (1/3)\mathcal{F}_{P33}$ for the η' , and $\mathcal{F}_{P88} = (-1/3)\mathcal{F}_{P33}$ for the η .

Table 13: Contributions to the $(2+2)_a$ diagrams $a_{\mu,(2+2)a}^{\text{HVP},38}(\Lambda)$ for $\Lambda = 16 m_\mu$ and $\Lambda = \infty$ at the $\text{SU}(3)_f$ symmetric point $M_\pi = M_K \simeq 416 \text{ MeV}$. All contributions in 10^{-11} units.

Contribution at $\text{SU}(3)_f$ point:	$a_{\mu,(2+2)a}^{\text{HVP},38}(\Lambda = 16 m_\mu)$	$a_{\mu,(2+2)a}^{\text{HVP},38}(\Lambda = \infty)$
charged pion & kaon loop	-0.27 (sQED)	-0.37 (VMD)
π^0 and η exchange	-0.42	-0.96
η' exchange	+0.16	+0.58
Total	-0.53	-0.75

At the $\text{SU}(3)_f$ symmetric point, the charged kaon loop gives the single largest contribution in absolute terms, imposing its negative sign on the total $a_{\mu,(2+2)a}^{\text{HVP},38}(\Lambda)$. At physical pion and kaon masses, we find that it is the π^0 exchange that dominates, resulting in a positive estimate for $a_{\mu,(2+2)a}^{\text{HVP},38}(\Lambda)$. Still, this estimate is very small, with $2 a_{\mu,(2+2)a}^{\text{HVP},38}(\Lambda)$ just below the 1×10^{-11} level.

Since in our lattice QCD calculation of $a_{\mu,(2+2)a}^{\text{HVP},38}$, the photon cutoff Λ is directly set to infinity, we cannot directly compare the model predictions of Table 12 to our lattice results. We therefore also use our model to estimate $a_{\mu,(2+2)a}^{\text{HVP},38}(\Lambda = 16 m_\mu)$: subtracting this contribution from our estimate of $a_{\mu,em}^{\text{HVP},38}(\Lambda = 16 m_\mu)$, we obtain a prediction for the connected contribution alone. In Table 13, we provide the predictions⁸ for $a_{\mu,(2+2)a}^{\text{HVP},38}(\Lambda = 16 m_\mu)$. For the connected contribution, we then obtain the estimate

$$a_{\mu,(4)}^{\text{HVP},38}(\Lambda) = a_{\mu,em}^{\text{HVP},38}(\Lambda) - a_{\mu,(2+2)a}^{\text{HVP},38}(\Lambda) \simeq +0.28(21) \times 10^{-11}, \quad \Lambda = 16 m_\mu, \quad (\text{D.1})$$

to which we attach an uncertainty of the typical size of an individual contribution such as the π^0 exchange. This value is to be compared to the continuum-extrapolated lattice QCD result provided in Table 4, $a_{\mu,(4)}^{\text{HVP},38}(\Lambda) = -0.25(32) \times 10^{-11}$. While this represents a difference at the level of 1.5σ , both the lattice result and the model estimate are very small and essentially compatible with zero.

For a hint as to where the slight tension comes from, we give the model prediction for $a_{\mu,(2+2)a}^{\text{HVP},38}(\Lambda = \infty)$ in the rightmost column of Table 13, which can be compared to the corresponding lattice result, Eq. (5.5). As already visible in figure 10a, the sum of the pseudoscalar exchanges already approximates the integrand quite well. This hints at the magnitude of the pseudoscalar loop contribution to $a_{\mu,(2+2)a}^{\text{HVP},38}(\infty)$ being overestimated by its evaluation using its matching factor of $1/6$ and a VMD form factor, or else at relevant positive contributions missing from our model. Similarly, the evaluation of the pseudoscalar loop contribution to $a_{\mu,(2+2)a}^{\text{HVP},38}(\Lambda = 16 m_\mu)$ using scalar QED likely yields an overestimate of its absolute value.

⁸In $a_{\mu,(2+2)a}^{\text{HVP},38}(\Lambda)$, the combined π_0 and η exchange comes with factor $-3/8$ and the η' exchange with factor $3/16$, relative to the size of these contributions in the full $a_{\mu,em}^{\text{HVP}}(\Lambda)$. The combined pion and kaon loop contribution comes with weight $1/12$ of its size in $a_{\mu,em}^{\text{HVP}}(\Lambda)$, to which the pion and the kaon loop make equal contributions.

D.2 Low-energy contribution $a_{\mu,em}^{\text{HVP},38,\text{low}}$

The pseudoscalar meson exchanges, as evaluated in the previous subsection with a transition form factor, remain UV-finite when $\Lambda \rightarrow \infty$. Upon introducing a VMD form factor in the evaluation of the kaon loop, the latter contribution also remains finite. Together, the PS meson exchanges and the kaon loop form the basis of our estimate of the low-energy contributions to $a_{\mu,em}^{\text{HVP},38,\text{low}}$, which is evaluated without a UV-cutoff on the photon propagator. The results at the $\text{SU}(3)_f$ and at the physical point are collected in Table 14.

At the $\text{SU}(3)_f$ symmetric point, the kaon loop tends to cancel very strongly against the η' exchange, while the π^0 and η exchanges cancel each other exactly. In total, $a_{\mu,em}^{\text{HVP},38,\text{low}}$ is practically zero. At the physical point, as noted in the previous subsection, the π^0 exchange dominates, but nevertheless remains a small contribution in comparison to the strong isospin-breaking contribution analyzed in the two coming subsections.

D.3 Elastic part of the kaon mass splitting

First of all, we use $\Delta M_K^{\text{phys}} = -3.9 \text{ MeV}$ in all cases. Secondly, we defined $\Delta M_K^{\text{elast}}$ as resulting from the elastic contribution to the forward Compton amplitude on the kaon. At the physical point, we borrow the (finite) estimate $\Delta M_K^{\text{elast}} = +2.1 \text{ MeV}$ based on the elastic contribution from [40]. At the $\text{SU}(3)_f$ point, the same master formula with a VMD form factor and a VMD mass of 860 MeV yields $\Delta M_K^{\text{elast}} = +2.4 \text{ MeV}$.

For comparison with the lattice, we also compute $\Delta M_K^{\text{elast}}$ with a regulated photon propagator ($\Lambda = 16 m_\mu$). The value of 1.53 MeV is reported in Table 11 and appears to saturate the lattice result for $\Delta M_K^{\text{em}}(\Lambda)$, suggesting that the inelastic contribution is still very small for this value of Λ .

The most important quantity to complete the prediction for the renormalized $a_\mu^{\text{HVP},38}$ is then R_{38K} .

D.4 Estimate of R_{38K} and $a_\mu^{\text{HVP},38}$ at the $\text{SU}(3)_f$ point

In order to estimate R_{38K} at the $\text{SU}(3)_f$ point, we note that the quark-mass derivative of $a_\mu^{\text{HVP},38}$ consists only of the three-point connected diagram, which can also be interpreted as a similar derivative within isosymmetric QCD:

$$\frac{\partial a_\mu^{\text{HVP},38}}{\partial(m_u - m_d)} = -\frac{3}{2} \frac{\partial a_\mu^{\text{HVP},88}}{\partial(m_l - m_s)} \Big|_{2m_l + m_s} = \frac{\partial a_\mu^{\text{HVP},88}}{\partial m_s} \Big|_{m_l} - \frac{1}{2} \frac{\partial a_\mu^{\text{HVP},88}}{\partial m_l} \Big|_{m_s}. \quad (\text{D.2})$$

In the second equality, we have only made use of the chain rule to change variables. At this point, we make the approximation that only the valence quarks of the relevant vector meson matter for estimating the quark-mass derivatives. Thus we arrive at

$$\frac{\partial a_\mu^{\text{HVP},38}}{\partial(m_u - m_d)} \simeq \frac{3}{4} \frac{\partial a_\mu^{\text{HVP},s}}{\partial m_s} \Big|_{m_l}. \quad (\text{D.3})$$

Note that the strangeness contribution $a_\mu^{\text{HVP},s}$ is defined to contain the charge factor of $(-1/3)^2$. We can now relate the expression to a mass derivative already modeled in [35],

Appendix B.2,

$$R_{38K} \simeq \frac{3}{2} M_K \left. \frac{\partial a_\mu^{\text{HVP},s}}{\partial M_K^2} \right|_{M_\pi^2}. \quad (\text{D.4})$$

In particular, we estimate the kaon mass dependence of the $\bar{s}s$ vector meson mass from

$$M_{ss}^V = M_\phi^{\text{phys}} + \left[\frac{M_\phi - M_\omega}{M_K^2 - M_\pi^2} \right]_{\text{phys}} (M_K^2 - \frac{1}{2} M_\pi^2 - (M_K^2 - \frac{1}{2} M_\pi^2)_{\text{phys}}). \quad (\text{D.5})$$

This expression returns the physical ϕ meson mass for physical (M_K, M_π) values, and the physical ω mass for $M_K = M_\pi = (M_\pi)_{\text{phys}}$. It delivers a successful prediction for the vector meson mass at the $\text{SU}(3)_f$ point as compared to a direct lattice calculation [36], in which the mass splitting between the octet and the singlet states is found to be small. Secondly, we neglect the dependence of the electronic width of vector mesons on the valence-quark mass [35, 51]. As in [35], we do however take into account the dependence of the perturbative threshold on the valence quark mass. Setting $M_\phi = 0.860 \text{ GeV}$ and $(9\pi/\alpha^2)\Gamma_{ee}(\phi) = 0.65 \text{ GeV}$ at our $\text{SU}(3)_f$ point, we obtain

$$R_{38K} = -1.53(38) \times 10^{-11} \text{ MeV}^{-1}. \quad (\text{D.6})$$

We have assigned a conservative uncertainty of 25% to the model (as compared to 15% in [35]), since we are applying it a distance away from the physical point, on which its parameter values are based. With this estimate of R_{38K} , we obtain

$$a_\mu^{\text{HVP},38} = 9.7(2.4)_{R_{38K}} (0.6)_{\text{em}} (0.6)_{\text{sd}} \times 10^{-11}. \quad (\text{D.7})$$

Our estimates of the bare e.m. contribution to $a_\mu^{\text{HVP},38}$ cancel almost completely, so that the final result arises solely from the counterterm. The uncertainties come, as indicated in the equation, from the estimate of R_{38K} ; from $a_{\mu,em}^{\text{HVP},38}$, to which we assign the size of the kaon loop as uncertainty to account for missing effects such as scalar, axial-vector and tensor meson exchanges; and from the short-distance contributions in the bare e.m. contribution, which must cancel against the short-distance contribution in the inelastic part of the e.m. kaon mass splitting. We have assigned an uncertainty to these short-distance parts given again by the size of the kaon loop, which has been computed with form factors.

D.5 Predicting R_{38K} and $a_\mu^{\text{HVP},38}$ at the physical point

The quantity R_{38K} is more subtle to estimate at the physical point, where one cannot make use of the $\text{SU}(3)_f$ symmetry. In that regime, the disconnected mass insertion plays an important role, canceling the dominant part of the connected three-point function [52]. In the derivative $\partial a_\mu^{\text{HVP},38} / \partial(m_u - m_d)$ at constant $(m_u + m_d)$ and m_s , due to the narrowness of the ω resonance, we expect a strong enhancement at $s \simeq M_\omega^2$. Since the mass operator $\bar{u}u - \bar{d}d$ carries no energy or momentum, of all the isovector final states the ρ resonance contribution is enhanced, since it has practically the same invariant mass as the ω resonance. Now, on resonance we expect the large- N_c behavior that the properties of

the resonances depend dominantly on their valence quarks. In that regime, we neglect the disconnected diagrams and write for the contributions from centre-of-mass energies $s \gtrsim M_\omega^2$,

$$\left. \frac{\partial a_\mu^{\text{HVP},38}}{\partial(m_u - m_d)} \right|_{m_u+m_d} \simeq \frac{3}{2} \left. \frac{\partial}{\partial m_l} \right|_{m_s} a_\mu^{\text{HVP},88}, \quad (\text{D.8})$$

where on the right-hand side the contribution of the strangeness current is neglected for the same large- N_c reasons. We then estimate by the same method as for the $\text{SU}(3)_f$ point above

$$m_l \left. \frac{\partial a_\mu^{\text{HVP},88}}{\partial m_l} \right|_{m_s} \simeq (-1.35 - 0.19) \times 10^{-10} = -1.54 \times 10^{-10}. \quad (\text{D.9})$$

In particular, the first term follows from the approximate relation

$$M_{ll}^V = M_\omega^{\text{phys}} + \frac{1}{2} \left[\frac{M_\phi - M_\omega}{M_K^2 - M_\pi^2} \right]_{\text{phys}} (M_\pi^2 - (M_\pi^{\text{phys}})^2) \quad (\text{D.10})$$

for the pion-mass dependence of the ω meson, while the second term corresponds to the quark-mass dependence of the threshold to a quasi-perturbative $\bar{q}q$ continuum. In this way, we arrive at

$$R_{38K} \simeq -2.50(63) \times 10^{-11} \text{ MeV}^{-1}. \quad (\text{D.11})$$

The quoted uncertainty of 25% comes from combining quadratically a 15% uncertainty for the estimate of the connected diagram and a 20% uncertainty for the non-accounted for contribution of the ω transition to the $\pi\pi$ continuum at energies below M_ρ . This continuum, whose relevance has already been pointed out in Ref. [48], also presents a certain challenge for lattice QCD, since it leads to a long-range contribution and presumably sizeable finite-volume effects in the calculation of R_{38K} .

The resulting counterterm C_T in the elastic approximation and the final model estimate of $a_\mu^{\text{HVP},38}$ are given in Table 12. Since the counterterm dominates, the uncertainty on $a_\mu^{\text{HVP},38}$ is again 25%. The total isospin-violating part of a_μ^{HVP} is thus estimated at

$$2 a_\mu^{\text{HVP},38} = 31.6(7.9) \times 10^{-11}. \quad (\text{D.12})$$

The strong isospin-breaking contribution to a_μ^{HVP} in the FLAG24 scheme [47] amounts to

$$a_{\mu,SIB}^{\text{HVP}} = 2 a_{\mu,SIB}^{\text{HVP},38} = -6 \text{ MeV} \times 2 R_{38K} = 30.0(7.5) \times 10^{-11}. \quad (\text{D.13})$$

This estimate is consistent within the errors with the previous result $33.2(8.9)$ [48], based on $\text{SU}(3)$ chiral perturbation theory as well as with the phenomenological estimate $a_{\mu,SIB}^{\text{HVP}} = 14.7(16.7) \times 10^{-11}$ [53].

Table 14: UV-finite contributions to $a_{\mu,em}^{\text{HVP},38}$ at physical quark masses, where $M_K = 494.6 \text{ MeV}$, and at the $\text{SU}(3)_f$ symmetric point $M_\pi = M_K \simeq 416 \text{ MeV}$. All contributions in 10^{-11} units.

	Contribution:	phys. point	$\text{SU}(3)_f$ point
$a_{\mu,em}^{\text{HVP},38,\text{low}}$:	K^+K^- (VMD)	-0.31	-0.56
	π^0 exchange	0.93	0.48
	η exchange	-0.24	-0.48
	η' exchange	0.44	0.58
	Total	0.81	0.01
$a_{\mu,SIB}^{\text{HVP},38}$:		15.0	9.7
$a_\mu^{\text{HVP},38}$:		15.8	9.7

References

- [1] D. Aguillard, T. Albahri, D. Allspach, A. Anisenkov, K. Badgley, S. Baeßler et al., *Measurement of the positive muon anomalous magnetic moment to 0.20 ppm*, *Phys. Rev. Lett.* **131** (2023) .
- [2] MUON G-2 collaboration, *Measurement of the Positive Muon Anomalous Magnetic Moment to 0.46 ppm*, *Phys. Rev. Lett.* **126** (2021) 141801 [2104.03281].
- [3] MUON G-2 collaboration, *Final Report of the Muon E821 Anomalous Magnetic Moment Measurement at BNL*, *Phys. Rev. D* **73** (2006) 072003 [hep-ex/0602035].
- [4] T. Aoyama et al., *The anomalous magnetic moment of the muon in the Standard Model*, *Phys. Rept.* **887** (2020) 1 [2006.04822].
- [5] R. Aliberti et al., *The anomalous magnetic moment of the muon in the Standard Model: an update*, 2505.21476.
- [6] W.N. Cottingham, *The neutron proton mass difference and electron scattering experiments*, *Annals Phys.* **25** (1963) 424.
- [7] J. Gasser and H. Leutwyler, *Implications of Scaling for the Proton - Neutron Mass Difference*, *Nucl. Phys. B* **94** (1975) 269.
- [8] V. Cirigliano, G. Ecker and H. Neufeld, *Radiative tau decay and the magnetic moment of the muon*, *JHEP* **08** (2002) 002 [hep-ph/0207310].
- [9] RM123 collaboration, *Leading isospin breaking effects on the lattice*, *Phys. Rev. D* **87** (2013) 114505 [1303.4896].
- [10] RBC, UKQCD collaboration, *Calculation of the hadronic vacuum polarization contribution to the muon anomalous magnetic moment*, *Phys. Rev. Lett.* **121** (2018) 022003 [1801.07224].
- [11] ETM collaboration, *Electromagnetic and strong isospin-breaking corrections to the muon $g - 2$ from Lattice QCD+QED*, *Phys. Rev.* **D99** (2019) 114502 [1901.10462].
- [12] S. Borsanyi et al., *Leading hadronic contribution to the muon magnetic moment from lattice QCD*, *Nature* **593** (2021) 51 [2002.12347].

- [13] G. Ray et al., *Calculating the QED correction to the hadronic vacuum polarisation on the lattice*, *PoS LATTICE2022* (2023) 329 [2212.12031].
- [14] D. Djukanovic, G. von Hippel, S. Kuberski, H.B. Meyer, N. Miller, K. Ottnad et al., *The hadronic vacuum polarization contribution to the muon $g - 2$ at long distances*, *JHEP* **04** (2025) 098 [2411.07969].
- [15] J. Parrino, V. Biloshytskyi, E.-H. Chao, H.B. Meyer and V. Pascalutsa, *Computing the UV-finite electromagnetic corrections to the hadronic vacuum polarization in the muon ($g - 2$) from lattice QCD*, [2501.03192](#).
- [16] A. Altherr et al., *Update on the isospin breaking corrections to the HVP with C-periodic boundary conditions*, in *41st International Symposium on Lattice Field Theory*, 2, 2025 [2502.14845].
- [17] RBC, UKQCD collaboration, *Hadronic light-by-light contribution to the muon anomaly from lattice QCD with infinite volume QED at physical pion mass*, *Phys. Rev. D* **111** (2025) 014501 [2304.04423].
- [18] E.-H. Chao, R.J. Hudspith, A. Gérardin, J.R. Green, H.B. Meyer and K. Ottnad, *Hadronic light-by-light contribution to $(g - 2)_\mu$ from lattice QCD: a complete calculation*, *Eur. Phys. J. C* **81** (2021) 651 [2104.02632].
- [19] Z. Fodor, A. Gerardin, L. Lellouch, K.K. Szabo, B.C. Toth and C. Zimmermann, *Hadronic light-by-light scattering contribution to the anomalous magnetic moment of the muon at the physical pion mass*, [2411.11719](#).
- [20] N. Kalntis, G. Kanwar, M. Petschlies, S. Romiti and U. Wenger, *Hadronic light-by-light contribution to the muon $g - 2$ using twisted-mass fermions*, [2412.12320](#).
- [21] M. Knecht, *The Anomalous magnetic moment of the muon: A Theoretical introduction*, *Lect. Notes Phys.* **629** (2004) 37 [hep-ph/0307239].
- [22] V. Biloshytskyi, E.-H. Chao, A. Gérardin, J.R. Green, F. Hagelstein, H.B. Meyer et al., *Forward light-by-light scattering and electromagnetic correction to hadronic vacuum polarization*, *JHEP* **03** (2023) 194 [2209.02149].
- [23] M. Hayakawa and S. Uno, *QED in finite volume and finite size scaling effect on electromagnetic properties of hadrons*, *Prog. Theor. Phys.* **120** (2008) 413 [0804.2044].
- [24] J. Bijnens, J. Harrison, N. Hermansson-Truedsson, T. Janowski, A. Jüttner and A. Portelli, *Electromagnetic finite-size effects to the hadronic vacuum polarization*, *Phys. Rev. D* **100** (2019) 014508 [1903.10591].
- [25] H.B. Meyer, *Lorentz-covariant coordinate-space representation of the leading hadronic contribution to the anomalous magnetic moment of the muon*, *Eur. Phys. J. C* **77** (2017) 616 [1706.01139].
- [26] M. Bruno et al., *Simulation of QCD with $N_f = 2 + 1$ flavors of non-perturbatively improved Wilson fermions*, *JHEP* **02** (2015) 043 [1411.3982].
- [27] E.-H. Chao, H.B. Meyer and J. Parrino, *Coordinate-space calculation of the window observable for the hadronic vacuum polarization contribution to $(g-2)_\mu$* , *Phys. Rev. D* **107** (2023) 054505 [2211.15581].
- [28] D. Bernecker and H.B. Meyer, *Vector Correlators in Lattice QCD: Methods and applications*, *Eur. Phys. J. A* **47** (2011) 148 [1107.4388].

- [29] M. Cè, A. Gérardin, K. Ottnad and H.B. Meyer, *The leading hadronic contribution to the running of the Weinberg angle using covariant coordinate-space methods*, *PoS LATTICE2018* (2018) 137 [[1811.08669](#)].
- [30] M. Bruno, T. Korzec and S. Schaefer, *Setting the scale for the CLS 2 + 1 flavor ensembles*, *Phys. Rev. D* **95** (2017) 074504 [[1608.08900](#)].
- [31] B. Strassberger et al., *Scale setting for CLS 2+1 simulations*, *PoS LATTICE2021* (2022) 135 [[2112.06696](#)].
- [32] RQCD collaboration, *Scale setting and the light baryon spectrum in $N_f = 2 + 1$ QCD with Wilson fermions*, *JHEP* **05** (2023) 035 [[2211.03744](#)].
- [33] S.N. et al. (Particle Data Group) *Phys. Rev. D* **110** (2024) 030001.
- [34] RQCD collaboration, *Lattice simulations with $N_f = 2 + 1$ improved Wilson fermions at a fixed strange quark mass*, *Phys. Rev. D* **94** (2016) 074501 [[1606.09039](#)].
- [35] M. Cè et al., *Window observable for the hadronic vacuum polarization contribution to the muon $g-2$ from lattice QCD*, *Phys. Rev. D* **106** (2022) 114502 [[2206.06582](#)].
- [36] E.-H. Chao, A. Gérardin, J.R. Green, R.J. Hudspith and H.B. Meyer, *Hadronic light-by-light contribution to $(g - 2)_\mu$ from lattice QCD with $SU(3)$ flavor symmetry*, *Eur. Phys. J. C* **80** (2020) 869 [[2006.16224](#)].
- [37] A. Gérardin, T. Harris and H.B. Meyer, *Nonperturbative renormalization and $O(a)$ -improvement of the nonsinglet vector current with $N_f = 2 + 1$ Wilson fermions and tree-level Symanzik improved gauge action*, *Phys. Rev. D* **99** (2019) 014519.
- [38] X. Feng and L. Jin, *QED self energies from lattice QCD without power-law finite-volume errors*, *Phys. Rev. D* **100** (2019) 094509 [[1812.09817](#)].
- [39] L. Maiani, G. Martinelli, M.L. Paciello and B. Taglienti, *Scalar Densities and Baryon Mass Differences in Lattice QCD With Wilson Fermions*, *Nucl. Phys. B* **293** (1987) 420.
- [40] D. Stamen, D. Hariharan, M. Hoferichter, B. Kubis and P. Stoffer, *Kaon electromagnetic form factors in dispersion theory*, *Eur. Phys. J. C* **82** (2022) 432 [[2202.11106](#)].
- [41] J. Koponen, D. Djukanovic, G. von Hippel, H.B. Meyer, K. Ottnad, T. Schulz et al., *Isvector Axial Form Factor of the Nucleon from Lattice QCD*, in *39th International Symposium on Lattice Field Theory*, 12, 2022 [[2212.01208](#)].
- [42] T. Bhattacharya, R. Gupta, W. Lee, S.R. Sharpe and J.M.S. Wu, *Improved bilinears in lattice QCD with non-degenerate quarks*, *Phys. Rev. D* **73** (2006) 034504 [[hep-lat/0511014](#)].
- [43] J. Heitger, F. Joswig, P.L.J. Petrak and A. Vladikas, *Ratio of flavour non-singlet and singlet scalar density renormalisation parameters in $N_f = 3$ QCD with Wilson quarks*, *Eur. Phys. J. C* **81** (2021) 606 [[2101.10969](#)].
- [44] M. Della Morte, A. Francis, V. Gülpers, G. Herdoíza, G. von Hippel, H. Horch et al., *The hadronic vacuum polarization contribution to the muon $g - 2$ from lattice QCD*, *JHEP* **10** (2017) 020 [[1705.01775](#)].
- [45] H. Bozdogan, *Model selection and akaike's information criterion (aic): The general theory and its analytical extensions*, *Psychometrika* **52** (1987) 345–370.
- [46] K. Kimura and H. Waki, *Minimization of akaike's information criterion in linear regression analysis via mixed integer nonlinear program*, *Optimization Methods and Software* **33** (2017) 633–649.

- [47] FLAVOUR LATTICE AVERAGING GROUP (FLAG) collaboration, *FLAG Review 2024*, [2411.04268](#).
- [48] C.L. James, R. Lewis and K. Maltman, *ChPT estimate of the strong-isospin-breaking contribution to the anomalous magnetic moment of the muon*, *Phys. Rev. D* **105** (2022) 053010 [[2109.13729](#)].
- [49] G. Colangelo, M. Hoferichter, B. Kubis and P. Stoffer, *Isospin-breaking effects in the two-pion contribution to hadronic vacuum polarization*, *JHEP* **10** (2022) 032 [[2208.08993](#)].
- [50] A. Gérardin, H.B. Meyer and A. Nyffeler, *Lattice calculation of the pion transition form factor with $N_f = 2 + 1$ Wilson quarks*, *Phys. Rev. D* **100** (2019) 034520 [[1903.09471](#)].
- [51] J.J. Sakurai, *Remarkable Regularity in the Lepton - Pair Widths of Vector Mesons*, *Physica A* **96** (1979) 300.
- [52] C. Lehner and A.S. Meyer, *Consistency of hadronic vacuum polarization between lattice QCD and the R-ratio*, *Phys. Rev. D* **101** (2020) 074515 [[2003.04177](#)].
- [53] M. Hoferichter, G. Colangelo, B.-L. Hoid, B. Kubis, J.R. de Elvira, D. Schuh et al., *Phenomenological Estimate of Isospin Breaking in Hadronic Vacuum Polarization*, *Phys. Rev. Lett.* **131** (2023) 161905 [[2307.02532](#)].